catalysts

MDPI

Review

A Mini-Review on Lanthanum–Nickel-Based Perovskite-Derived Catalysts for Hydrogen Production via the Dry Reforming of Methane (DRM)

Amvrosios G. Georgiadis, Nikolaos D. Charisiou and Maria A. Goula *

Laboratory of Alternative Fuels and Environmental Catalysis (LAFEC), Department of Chemical Engineering, University of Western Macedonia, GR-50100 Kozani, Greece; amvro23@gmail.com (A.G.G.); ncharisiou@uowm.gr (N.D.C.)

* Correspondence: mgoula@uowm.gr; Tel.: +30-24610-66651

Abstract: Given that the attempts to head toward a hydrogen economy are gathering pace, the dry reforming of methane (DRM) to produce hydrogen-rich syngas is a reaction that is worthy of investigation. Nickel-based catalysts have been extensively examined as a cost-effective solution for DRM, though they suffer from fast deactivation caused by coke accumulation. However, a number of published studies report high catalytic performance in terms of both activity and stability for La–Ni-based perovskite-derived catalysts used in DRM in comparison to other corresponding materials. In the work presented herein, a thorough analysis regarding the application of La–Ni-based perovskite catalysts for DRM is carried out. $LaNiO_3$ is known for its anti-coking ability owing to the strong interaction between CO_2 and La_2O_3. A further modification to improve the catalytic performance can be achieved by the partial or complete substitution of A or/and B sites of the perovskite catalysts. The latest developments with respect to this topic are also discussed in this manuscript. Even though the low surface area of perovskite catalysts has always been an obstacle for their commercialization, new supported and porous perovskite materials have recently emerged to address, at least partly, the challenge. Finally, conclusions and future outlooks for developing novel perovskite catalysts that may potentially pioneer new technology are included.

Keywords: dry reforming of methane; perovskites; La–Ni-based perovskites; exsolution; $LaNiO_3$; kinetics

check for updates

Citation: Georgiadis, A.G.; Charisiou, N.D.; Goula, M.A. A Mini-Review on Lanthanum–Nickel-Based Perovskite-Derived Catalysts for Hydrogen Production via the Dry Reforming of Methane (DRM). *Catalysts* **2023**, *13*, 1357. https://doi.org/10.3390/catal13101357

Academic Editors: Shian Li and Qiuwan Shen

Received: 22 September 2023
Revised: 3 October 2023
Accepted: 7 October 2023
Published: 10 October 2023

Copyright: © 2023 by the authors. Licensee MDPI, Basel, Switzerland. This article is an open access article distributed under the terms and conditions of the Creative Commons Attribution (CC BY) license (https://creativecommons.org/licenses/by/4.0/).

1. Introduction

Energy holds a prominent role in modern societies, and the increase in world population and living standards will inevitably lead to further rises in the energy demand [1]. However, even though tremendous effort has been put toward developing renewable energy sources (RESs), fossil fuels are still responsible for nearly 80% of global energy consumption, with the remaining 20% also including nuclear and large-scale hydropower [2,3]. Because of the energy model followed for the past 200 years, the concentration of carbon dioxide (CO_2) has been steadily rising (it stood at around 419 ppm by June 2021 [4]), driving the continual increase in global surface and ocean temperatures [5,6]. Global warming, in turn, is responsible for climate change, which threatens human societies worldwide with catastrophic consequences [7,8].

A potential candidate to replace fossil fuels that is attracting increasing attention in the development of future energy systems is hydrogen [9–12]. Hydrogen has the major advantage of being a clean burning molecule, and its versatility means that it can facilitate the decarbonization of a range of sectors that have proved difficult to clean up in the past. This includes industries such as iron and steel, as well as transportation, especially long haul [13,14]. Hydrogen can also be employed to heat homes and store renewable electricity

that would otherwise be wasted [15–17]. Another advantage is that hydrogen can also be produced from renewable feedstocks such as biomass [18–20].

Today, the annual worldwide hydrogen consumption is approximately 0.4–0.5 billion Nm^3 [21]. Hydrogen production through the natural gas reforming process, which accounts for nearly 80–85% of the global hydrogen production, is advantageous because there is no need for investment in facilities or transport. In general, reforming processes include dry, steam, bi-, tri-, or partial oxidation, depending on the co-reactants (oxidizing agents). Among these methods, the dry reforming of methane (DRM) with carbon dioxide (Equation (1)) has the added advantage of consuming the main greenhouse gases (i.e., CH_4 and CO_2). The process produces syngas, which is a chemical building block for many petrochemical and refining processes. Syngas can be converted into valuable hydrocarbon products via Fischer–Tropsch (FT) synthesis or by CO separation into H_2 [22,23].

$$CH_4 + CO_2 \rightarrow 2CO + 2H_2 \ \Delta H^o{}_{298K} = 247.3 \text{ kJmol}^{-1} \quad (1)$$

Moreover, DRM offers a lower carbon footprint in comparison to other conventional methods for methane conversion to syngas (e.g., steam reforming) and, as result, can lower the net emissions of the CO_2 and CH_4 gases, especially if the energy used for it comes from non-hydrocarbon sources (e.g., solar energy) [24–26]. Despite its obvious attractions, DRM has yet to be fully commercialized owing to certain challenges and limitations that need to be addressed. For example, the reaction is carried out at very high temperatures because of its high endothermicity, which significantly increases the energy costs [27,28]. Moreover, even though numerous conventional metal/support catalytic systems have been shown to exhibit high catalytic activity, deactivation, owing to rapid carbon deposition on the catalyst, and the sintering of the metals that constitute the active phase remain obstacles yet to be surmounted [29,30].

Perovskites are one of the most common crystal structures found on the planet, making up 93% of the lower mantle's mass, and 38% of the total mass of the planet. While it was originally discovered as a mineral, this crystal shape shows up everywhere and is a common subject for cutting-edge scientific research [31]. There are several different kinds of perovskites, namely $CaTiO_3$, $BaTiO_3$, $CaSiO_3$, and $MgSiO_3$, but they share a similar, dense crystalline structure. Nowadays, this class of materials has received considerable attention because such materials have been used in many areas, including heterogeneous catalysis [32–34].

In the last years, the use of perovskite-based catalysts for the dry reforming of methane has been growing rapidly, and a significant number of related scientific articles have been published. However, when searching through the available literature, one can find only a handful of review papers focusing on the use of perovskites in the DRM reaction [35,36]. This work focused exclusively on the use of lanthanum–nickel-based perovskite-derived catalysts for use in the DRM reaction, also presenting information with respect to kinetic and mechanistic aspects. It is hoped that, by highlighting the enhanced catalytic properties of these materials in the DRM, we will contribute to the discussion on the improvement of their structural characteristics and, resultantly, help them to achieve a higher catalytic performance.

2. Brief Summary of Ni-Based Catalysts for Methane Dry Reforming

A plethora of different metal-supported catalysts have been used for the DRM, with nickel-based systems showing comparative advantage over several noble-metal-based systems (e.g., Ru and Rh) due to the cost effectiveness of such formulations. As an example, Hou et al. [37] showed that Ni/Al_2O_3 exhibited increased initial activity compared to noble metal catalysts; however, its activity was compromised owing to carbon deposition. The same group also reported a beneficial synergetic effect between Ru and nickel that drastically reduced carbon deposition and enhanced catalytic activity.

As is well understood, different side reactions, such as the Reverse Water–Gas Shift (RWGS) (Equation (2)), CH_4 decomposition (Equation (3)), and CO disproportionation or Boudouard reaction (Equation (4)), synchronously take place during the DRM.

$$CO_2 + H_2 \rightarrow CO + H_2O,\ \Delta H^o{}_{298K} = 41\ \text{kJmol}^{-1} \quad (2)$$

$$CH_4 \rightarrow C_{ads} + 2H_2,\ \Delta H^o{}_{298K} = 75\ \text{kJmol}^{-1} \quad (3)$$

$$2CO \rightarrow C_{ads} + CO_2,\ \Delta H^o{}_{298K} = -172\ \text{kJmol}^{-1} \quad (4)$$

A major issue for the DRM is the absence of oxygen, which does not allow for the gasification of the carbon formed by the Boudouard and methane-cracking reactions. Consequently, the catalysts used in the DRM often suffer from heavy carbon accumulation, which shortens their lifetime [29,30,38]. The Boudouard reaction is not favored thermodynamically at high temperatures (above 800 °C), as it is highly exothermic; hence, the carbon formed beyond this limit is mainly due to methane cracking [39–41]. However, as carbon species generated from methane cracking are more reactive in comparison to those produced by the Boudouard reaction, they can be oxidized by carbon dioxide; thus, coke accumulation beyond 800 °C is relatively insignificant [42–44]. Nevertheless, at a lower temperature range, the carbon species formed by the Boudouard reaction are not that active, meaning that carbon deposition is facilitated [45–47].

Along these lines, the development of a stable, highly carbon resistant nickel-based catalyst is a critical issue. Thus far, it is well known that the size of nickel metal particles plays a key role in carbon deposition. However, the nickel nanoparticles are prone to thermal sintering due to the low Tammann temperature of the metallic nickel [48,49]. Consequently, stabilization of the supported nickel particles to avoid their agglomeration is a matter of great importance. In addition, the surface structure of Ni particles also affects the carbon deposition. Specifically, Wang et al. [50] reported that CH_4 decomposition occurs faster on the surface of nickel (100) and nickel (110) in comparison to nickel (111) probably because the preferential catalytic pathway on different surfaces varies. Differences can also be found regarding the segregation behavior and diffusion of carbon atoms. For instance, it is easier for the diffusion of surficial carbon to take place in the bulk of nickel (110) compared to that of nickel (100) [51]. Thus, it is generally accepted that one of the most important factors for eliminating carbon deposition is associated with metal surface modifications. For example, it has been reported for phyllosilicate-derived materials that are used as catalysts for the DRM that a significant number of hydroxyl radicals on the support surface can promote H_2O activation, as well as gasify carbon species on the adjacent nickel surface [52–54].

Several techniques by different scientific groups have been developed to transfuse higher carbon resistance and reduce carbon deposition [55,56]. For this purpose, materials with different structures, such as phyllosilicates [30,52,54,57], spinel [58–60], and perovskites [61–65], have been widely used as catalyst precursors.

Perovskite-based catalysts for DRM have been thoroughly investigated in recent years and have been addressed in an increasing number of publications. The reason why they are so popular lies in fact that the exsolution taking place during the reduction of perovskite-based catalysts can provide a strong metal–support interaction and resistance to particle aggregation to alleviate their deactivation. In short, during exsolution, transition metal dopants are reduced to the elemental state, and metal nanoparticles emerge from the oxide structure, forming supported metal catalysts which are strongly anchored in the parental matrix. Those that are strongly socketed in the support nanoparticles are endowed with anti-coking properties, making them great candidates for long-term operations. In addition, numerous studies have shown that exsolution is cyclable, meaning that the metal nanoparticles are able to dissolve and return to being dopants in the oxide matrix and then regenerate on the material surface following a second reduction treatment [60,62,66–69].

The work presented herein attempts to make a constructive contribution to the existing literature by providing updated and clear information on the subject under consideration.

3. Perovskites for DRM

Generally speaking, a perovskite is a material that has a structural formula of ABO_3 (Figure 1), where A is a large cation (i.e., lanthanides, alkaline, or alkaline earth metals) that is 12-fold coordinated, B is a small cation (i.e., 6-fold coordinated) of the d-transition series, and O is an anion that bonds to both [70,71]. A_2BO_4 oxides (Figure 1) belong to the Ruddlesden–Popper (RP) phases (i.e., subclass of layered perovskite materials), and they are composed of alternating ABO_3 and AO layers; A_2BO_4 are also referred to as perovskite in many scientific works [71]. Owing to their unique structural characteristics, they can accommodate the majority of the metals at A and/or B sites without damaging the crystallinity of the structure [72,73]. In addition, perovskites feature high thermal stability, making them ideal choices for gas-phase reactions carried out at high temperatures, as well as increased oxygen mobility, which has a significant influence on eliminating coke formation during DRM [74–76].

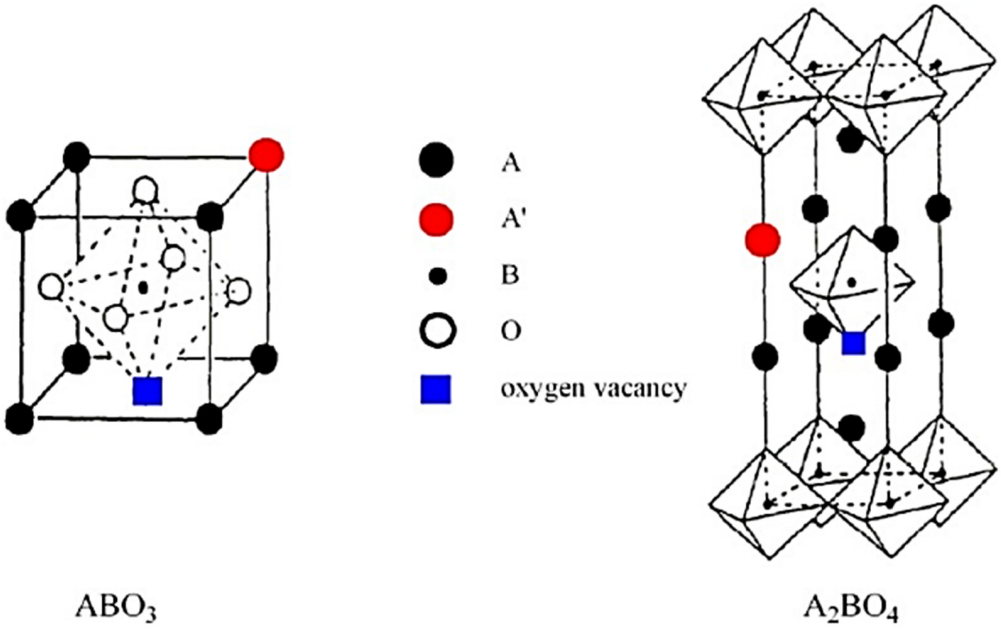


Figure 1. Ideal model of perovskite-type oxides ABO_3 (**left**) and A_2BO_4 (**right**). Reproduced with permission from Ref. [71]. Copyright 2014, *ACS Catalysis*.

DRM can be catalyzed by nickel; thereby, Ni-containing perovskite oxides can serve as precursors for DRM. Following hydrogen-reduction pretreatment, nickel cations are reduced to their active metal form (Ni^0). However, the coexistence of additional metals at A or/and B sites can be challenging, as mixed oxides or/and bimetallic particles may be generated. In the following subsections, the perovskite-based catalysts are going to be grouped in accordance with their basic ABO_3 type, as well as their A- and B-site substitution. In addition, considering that an excellent review of the synthesis and characterization methods of perovskite has already been published, only a brief summary of the effect of the preparation method on catalytic performance for this type of materials is presented in this paper [71].

3.1. La–Ni Perovskite-Derived Catalysts for DRM

The most widespread nickel-based perovskite oxide used as a precursor for DRM is $LaNiO_3$. One of the earliest works reported by Verykios and co-workers [77] showed that a $LaNiO_3$ catalyst had a stable performance during time on stream, in contrast with conventional Ni-based catalysts, whose performance declined over time. Provendier et al. [78] also

showed considerably high initial activity for a $LaNiO_3$ sample synthesized via a sol–gel method; however, carbon formation led to rapid deactivation. The authors also observed that the inclusion of small amounts of Fe to the perovskite structure significantly enhanced (to approximately 200 h) the stability of the sample without substantially compromising the activity. Over a decade later, Batiot-Dupeyrat et al. [79] reported that a $LaNiO_3$, which was synthesized via the auto-ignition method, was stable at 700 °C (90% conversion of reactants) during a time-on-stream test of 100 h (Figure 2). Another more recent study was carried out by Cao et al. [80], who showed that $LaNiO_3$ maintained a stable performance at different cycling stages.

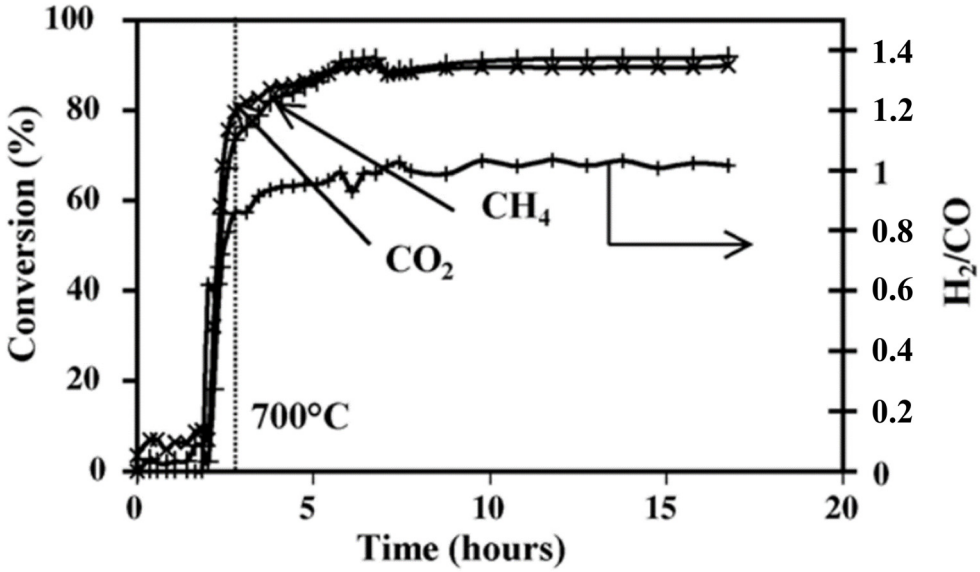


Figure 2. CH_4 and CO_2 conversions and H_2/CO ratio using $LaNiO_3$ DRM at 700 °C versus time. Reproduced with permission from Ref. [79]. Copyright 2005, *Catalysis Today*.

In another noteworthy work carried out by Batiot-Dupeyrat et al. [81], the authors studied preactivated/reduced $LaNiO_3$ materials synthesized via the explosion method and found that the catalysts were stable during time-on-stream runs, showing low carbon deposition. The authors also argued that the formation of La_2NiO_4 (spinel structure) acted as an intermediate product participating in the DRM. In addition, the authors observed the formation of NiO and La_2NiO_4 following the oxidation of the spent $LaNiO_3$; however, the original perovskite structure was not reinstated. Using the self-combustion method, Gallego et al. [82] also synthesized a stable Ni/La_2O_3 catalyst, which was derived through the reduction of a $LaNiO_3$ precursor. This group also showed that La_2NiO_4 outperformed $LaNiO_3$ in terms of catalytic activity at 700 °C. In a similar work, Gallego et al. [83] prepared $LaNiO_3$ and La_2NiO_4 via the wet impregnation method and reported higher activity for the former perovskite in comparison to that of the latter perovskite, a fact that was assigned to the incomplete nickel reduction at lower temperatures (i.e., 500 °C). The authors denoted that the generation of slightly small nickel particles during hydrogen reduction increased the catalytic activity of the perovskites. Furthermore, the concurrent occurrence of RWGS resulted in lower CO_2 conversions compared to CH_4 conversions. On the other hand, the H_2/CO ratio was close to unity due to another simultaneous side reaction (i.e., CH_4 decomposition) that counterbalanced the hydrogen consumed from RWGS.

A noteworthy work was conducted by Pereñiguez et al. [84], who investigated the effect of different preparation methods, namely spray pyrolysis, spray pyrolysis–combustion, combustion, and hydrothermal synthesis, on the catalytic performance and physicochemical behavior of $LaNiO_3$ for DRM. It was shown that $LaNiO_3$ prepared through combustion performed poorly in comparison to that obtained through the other three methods, probably owing to the participation of increased levels of the NiO phase in the pristine calcined

sample. Typically, larger Ni^0 particle clusters obtained from the NiO phase during hydrogen pretreatment can weaken metal–support interactions and resultantly compromise catalytic performance. Furthermore, it was shown that the spray-pyrolysis–combustion method resulted in well-formed $LaNiO_3$ nanocrystals, which, in addition to producing catalysts with high porosity comprising small $LaNiO_3$ nanocrystals agglomerates, suppressed sintering phenomena during calcination. It is also worth noticing the considerable higher surface area values of the obtained perovskites in comparison to the ones reported in the literature. Another interesting study was conducted by Chawla et al. [85], who reported higher reactant conversions for $LaNiO_3$ perovskites prepared through the coprecipitation method when evaluated against sol–gel-prepared ones.

Typically, hydrogen temperature-programmed reduction (TPR) profiles of $LaNiO_3$ perovskites show two main reduction peaks for nickel at two different temperature ranges (i.e., 300–450 °C and 500–600 °C, respectively), as shown in Figure 3 [86].

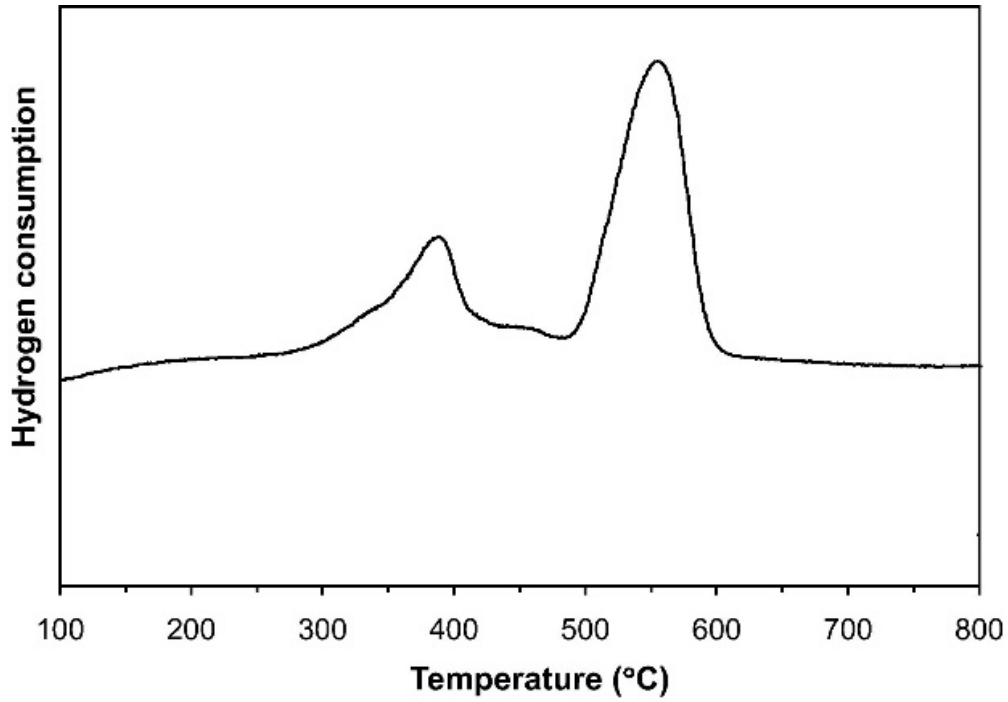


Figure 3. Hydrogen TPR profile of $LaNiO_3$. Reproduced with permission from Ref. [86]. Copyright 2011, *Catalysis Today*.

One of the most widely accepted reduction pathways for $LaNiO_3$ was introduced by Kuras et al. [87], shown in Equations (5) and (6) below.

$$2LaNiO_3 + H_2 \rightarrow La_2Ni_2O_5 + H_2O\ (Low\ peak) \quad (5)$$

$$La_2Ni_2O_5 + 2H_2 \rightarrow 2Ni^0 + La_2O_3 + 2H_2O\ (High\ peak) \quad (6)$$

Valderrama et al. [88] corroborated the detection of a $La_2Ni_2O_5$ intermediate phase under a hydrogen atmosphere, using X-ray diffraction (XRD) analysis.

On the other hand, a three-step reduction pathway for $LaNiO_3$ was proposed by Batiot-Duperyrat et al. [81], as shown below.

$$4LaNiO_3 + 2H_2 \rightarrow La_4Ni_3O_{10} + Ni^0 + 2H_2O \quad (7)$$

$$LaNiO_3 + 3H_2 \rightarrow La_2ONi_4 + 2Ni^0 + La_2O_3 + 3H_2O \quad (8)$$

$$La_2ONi_4 + H_2 \rightarrow Ni^0 + La_2O_3 + H_2O \quad (9)$$

In a more recent study, Papargyriou et al. [89] proposed a more generalized reduction pathway which considers the phase change to various Ruddlesden–Popper phases ($A_{m+1}B_mO_{3m+1}$) under hydrogen atmosphere. The potential differences that occurred can be assigned to the calcination and preparation conditions, as well as the promoters used to synthesize the materials.

The evidently lower reducibility of nickel in $LaNiO_3$ compared to conventional supported catalysts suggests a more solid interaction in the perovskite framework between nickel atoms and lanthanum oxide, which, in turn, limits thermal agglomeration during hydrogen pretreatment, generating highly dispersed nickel particles (Ni^0) on A-cation oxide.

The exceptional carbon-resistant properties of $LaNiO_3$ in DRM have been thoroughly discussed by numerous relevant studies, in which both preparation and pretreatment methods played a crucial role in the catalytic performance [69,88,90–93].

Another important determinant of catalytic behavior is the particle size of active metal. Chai et al. [94] prepared a nickel-doped $La_{0.46}Sr_{0.34}Ti_{0.9}Ni_{0.1}O_3$ catalyst with two different-sized nickel particles. The reduction of weakly interacting surface NiO at temperatures lower than 700 °C led to the formation of larger nickel particles (almost 14 nm), while the nickel incorporation into the perovskite structure at temperatures greater than 900 °C resulted in smaller nickel particles. DRM tests were carried out at 700 °C, using catalysts reduced at different temperatures. The authors noted increased catalytic activity and stability for the samples (active for 100 h) reduced at 950 °C, probably because of the presence of smaller nickel particles, which are known for their coke-resistant properties.

Pereñiguez et al. [95] managed to prepare $LaNiO_3$ samples, using the spray pyrolysis method, with nickel particles that were highly resistant to oxidation even after several cycles. A temperature-programmed oxidation (TPO) analysis of the reduced samples suggested similar oxidation profiles (OPs) for all the samples (Figure 4): (a) is the OP of pristine reduced $LaNiO_3$, (b) is the OP of pristine reduced $LaNiO_3$ after one TPR-TPO cycle, and (c) is the OP of pristine reduced $LaNiO_3$ after two TPR-TPO cycles.

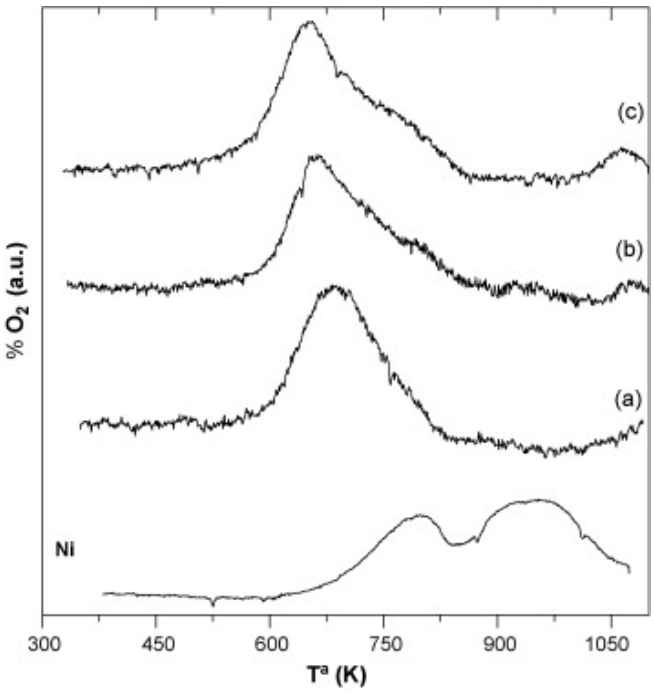


Figure 4. $LaNiO_3$ TPO profiles following reduction at 800 °C. Reproduced with permission from Ref. [95]. Copyright 2010, *Applied Catalysis B: Environmental*.

The appearance of a change in the maximum peak at decreased temperatures (profile (a) to profile (c)) can be assigned to the higher dispersion due to a reduction in the nickel particle (Ni^0) size. Furthermore, smaller metallic particles can be easier to oxidize in comparison to their larger counterparts.

The literature shows that La–Ni-containing perovskite oxides were the most popular catalysts for DRM reaction, whereas only a few other combinations with nickel in the structure were investigated recently. For example, Dama et al. [96] prepared $MZr_{0.8}Ni_{0.2}O_{3-\delta}$ (M = Ba, Sr, Ca) perovskites synthesized by a conventional sol–gel method for DRM at 800 °C. The authors noted that Ca-containing sample exhibited high activity and stability during a time-on-stream test of 500 h, suggesting potential for commercial exploitation. The catalyst's stability was assigned to the redox property of the support which facilitated coke removal.

3.2. $A_1A_2BO_3$ Perovskite Catalysts

$LaNiO_3$ can be modified via the partial substitution of the A site with other metals to obtain the $M_xL_{1-x}NiO_3$ form. Research that focusses on finding the appropriate element and identifying the ideal substituted quantity is crucial to obtain a high catalytic performance. Table 1 summarizes the related research.

Table 1. $A_1A_2BO_3$ perovskite catalysts for DRM.

Perovskite	Operating Conditions	CH_4 Conversion Order	Carbon Deposition	Ref.
$La_{0.95}Ba_{0.05}NiO_3$ $La_{0.90}Ba_{0.10}NiO_3$ $La_{0.85}Ba_{0.15}NiO_3$ $La_{0.80}Ba_{0.20}NiO_3$ $La_{0.75}Ba_{0.25}NiO_3$ $La_{0.70}Ba_{0.30}NiO_3$	T = 650–750 °C WHSV = 60,000 mL g^{-1} h^{-1} CH_4:CO_2:He = 1:1:8	$La_{0.90}Ba_{0.10}NiO_3$ > $La_{0.85}Ba_{0.15}NiO_3$~$La_{0.85}Ba_{0.15}NiO_3$ > $La_{0.75}Ba_{0.25}NiO_3$ > $La_{0.70}Ba_{0.30}NiO_3$ Ba-substituted catalysts outperformed the Sr and Mg ones.	-	[97]
$LaNiO_3$ $La_{0.95}Ca_{0.05}NiO_3$ $La_{0.90}Ca_{0.10}NiO_3$ $La_{0.70}Ca_{0.30}NiO_3$ $La_{0.50}Ca_{0.50}NiO_3$ $La_{0.20}Ca_{0.80}NiO_3$	T = 650–750 °C WHSV = 720,000 mL g^{-1} h^{-1} CH_4:CO_2 = 1:1	$La_{0.50}Ca_{0.50}NiO_3$~$La_{0.70}Ca_{0.30}NiO_3$ > $La_{0.95}Ca_{0.05}NiO_3$ > $La_{0.20}Ca_{0.80}NiO_3$ > $La_{0.90}Ca_{0.10}NiO_3$ > $LaNiO_3$	-	[98]
$LaNiO_3$ $La_{0.9}Sr_{0.1}NiO_3$ $La_{0.8}Sr_{0.2}NiO_3$ $La_{0.7}Sr_{0.3}NiO_3$ $La_{0.6}Sr_{0.4}NiO_3$ $Ni(5\%)/La_2O_3$	T = 700 °C CH_4:CO_2 = 1:1	$LaNiO_3$ > $La_{0.6}Sr_{0.4}NiO_3$ > $Ni(5\%)/La_2O_3$ > $La_{0.9}Sr_{0.1}NiO_3$ The order of activity depends on the content of strontium.	no coke no coke no coke no coke no coke no coke	[88]
$La_2Ni_{0.3}Al_{0.7}O_3$ $La_{0.8}Sr_{0.2}Ni_{0.3}Al_{0.7}O_{2.9}$ $La_{0.5}Sr_{0.5}Ni_{0.3}Al_{0.7}O_{2.75}$ $La_{0.2}Sr_{0.8}$ $Ni_{0.3}Al_{0.7}O_{2.6}$	T = 750 °C WHSV = 15,000 mL g^{-1} h^{-1} CH_4:CO_2:N_2 = 1:1:8	$La_{0.2}Sr_{0.8}$ $Ni_{0.3}Al_{0.7}O_{2.6}$ > $La_{0.5}Sr_{0.5}Ni_{0.3}Al_{0.7}O_{2.75}$ > $La_{0.8}Sr_{0.2}Ni_{0.3}Al_{0.7}O_{2.9}$ Ca-substituted catalysts were more stable but less active.	8.71%—15 h 8.31%—15 h 3.21%—15 h -	[99]
$LaNiO_3$ $La_{0.98}Pr_{0.02}NiO_3$ $La_{0.90}Pr_{0.10}NiO_3$ $La_{0.60}Pr_{0.40}NiO_3$	T = 700 °C WHSV = 600,000 mL g^{-1} h^{-1} CH_4:CO_2 = 1:1	$La_{0.50}Pr_{0.10}NiO_3$ > $LaNiO_3$ > $La_{0.98}Pr_{0.02}NiO_3$ > $La_{0.60}Pr_{0.40}NiO_3$	63%—8 h 51%—8 h traces—8 h 52%—8 h	[100]
$LaNiO_3$ $La_{0.90}Ce_{0.10}NiO_3$ $La_{0.70}Ce_{0.30}NiO_3$ $La_{0.50}Ce_{0.50}NiO_3$	T = 600–800 °C GHSV = 10,000 h^{-1} CH_4:CO_2 = 1:1	$LaNiO_3$ > $La_{0.90}Ce_{0.10}NiO_3$ > $La_{0.50}Ce_{0.50}NiO_3$ > $La_{0.70}Ce_{0.30}NiO_3$	-	[101]

Moradi et al. [97] compared the catalytic performance for the DRM of three different $La_{1-x}M_xNiO_3$-type (M = Ca, Sr, and Ba) perovskites. The results suggested that the Ba-containing sample outperformed the other tested catalysts in terms of catalytic activity. Next, the authors tried to evaluate the effect of Ba promotor ($5\% \leq x \leq 30\%$) on the catalytic performance and found that 20% of Ba offered the optimum promotion effect. De Lima et al. [98] investigated the substitution of calcium, drawing similar conclusions. The authors reported a promotion effect when a certain amount of Ca was added onto the substituted catalysts. On the other hand, beyond that calcium threshold, a high concentration of calcium can be accumulated on the surface, consequently compromising this promotion effect.

Lima et al. [102] investigated ceria-substituted perovskites in the DRM reaction. The authors reported that significant amounts of La_2NiO_4, CeO, and NiO were segregated due to the low solubility of ceria in the $La_{1-x}Ce_xNiO_3$ matrix when $x > 0.4$. The optimum amount of ceria to produce the most active catalyst was found to be $x = 0.05$; meanwhile, increasing the value of x beyond that threshold led to lower activities. Moreover, the redox chemistry of the ceria oxide, which was produced after the reduction of the perovskite oxide, created oxygen vacancies that hindered the coke formation during DRM. Similarly, Gallego et al. [100] showed that the existence of highly dispersed and easily reducible nanosized nickel particles in ceria-substituted perovskites resulted in increased catalytic activity. The substitution of the bigger lanthanum by the smaller ceria affected the structural stability of the material, assisting in improved reducibility. In addition, the redox chemistry of ceria promoted the oxidation of carbon species. Another study that focused on the importance of oxygen vacancies resulting from the addition of ceria in a perovskite matrix was conducted by Wang et al. [103]. Interestingly, it was reported that the oxygen vacancies in the perovskite structure were created indirectly by the activation of B-site cations, since the valency state of ceria is the same as that of the A site. Firstly, the group employed a sol–gel self-combustion method to prepare a series of $La_{1-x}Ce_xNi_{0.5}Fe_{0.5}O_3$ perovskites. Next, a TPR analysis was performed to evaluate the activity of the materials with respect to reducibility. Figure 5 shows the TPR profiles of the pristine sample with different x-values. Along these lines, peaks 1, 2, and 3 represent the reduction of nickel and iron species. It can be seen that these peaks shifted to lower temperatures as the x-values increased, suggesting that the addition of ceria at a site facilitated the reducibility process. On the other hand, peaks 4 and 5 correspond to reduced NiO and $NiFe_2O_4$ phases, as the perovskite structure was not formed when $x > 0.6$. Su et al. [101] also reported that lower ceria content resulted in higher catalytic activity. It was shown that $La_{0.9}Ce_{0.1}NiO_3$ was the optimized catalyst due to the increased number of oxygen atoms, as confirmed by the TPR results.

Lanthanides such as praseodymium (Pr) and samarium (Sm) can also be incorporated to substitute for lanthanum, either completely or partially, at the A site to produce a perovskite structure. These oxides have the ability to generate oxygen vacancies, enhancing the activity and durability of catalytic systems [104,105]. Gallego et al. [100] tested praseodymium (Pr)- and ceria (Ce)-substituted catalysts for DRM and showed that their addition facilitated the reduction process, as corroborated by the TPR results. It was also noted that the inclusion of either praseodymium or ceria could significantly reduce carbon deposition. $La_{0.9}Pr_{0.1}NiO_3$ had the best catalytic behavior, a fact that was assigned to the redox potential of Pr_2O_3 and the small (6 nm) nickel particles.

Sr-substituted perovskites were investigated even more thoroughly. Yang et al. [106] mentioned that the $La_2O_2CO_3$ surface was homogeneously covered by strontium species, resulting in a less strong metal–support interaction. Along these lines, the larger nickel particles obtained resulted in lower methane conversions. Nevertheless, the substitution of Sr improved the perovskite's carbon resistance since CO_2 and CH_4 activation was promoted. These results were in line with Rynkowski's relevant study [107]. Valderrama et al. [88] reported that the partial substitution of lanthanum by strontium in the perovskite matrix decreased the oxidation state of nickel, facilitating its reduction and producing spinel-structured solids owing to the increase in vacancies that promoted the oxygen mobility

toward the surface of the catalyst. Sutthiumporn et al. [47] studied the effect of alkaline earth metal promoter over Ni/La_2O_3. X-ray photoelectron spectroscopy (XPS), temperature-programmed desorption (O-TPD), and H_2-TPR characterizations showed the existence of surface oxygen vacancies on substituted perovskites (M = Sr, Ca, and Mg), which consecutively promoted CO_2 adsorption/desorption in the samples. Firstly, the authors mentioned the importance of the $La_2O_2CO_3$ intermediate phase, which was found in La-based perovskites, in oxidizing surface carbon. Next, the group reported that the Sr-substituted catalyst had the highest CH_4 and CO_2 conversion, as well as the smallest amount of coke formation. The addition of strontium caused a lattice distortion and valence imbalance (Sr^{2+} and La^{3+}), which led to an oxygen defect, thus increasing the lattice oxygen. The increased amount of lattice oxygen, in turn, can promote C–H activation, and it can react with carbon species, which improves the anti-coking properties of the perovskite.

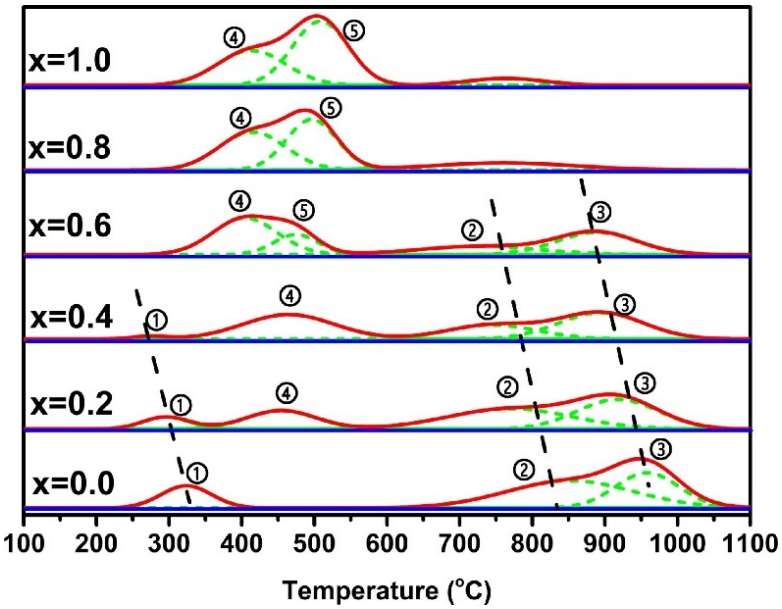


Figure 5. TPR profiles of pristine $La_{1-x}Ce_xNi_{0.5}Fe_{0.5}O_3$ with varying x-values. Reproduced with permission from Ref. [103]. Copyright 2018, *Applied Catalysis B: Environmental*.

Wang et al. [50] theoretically approached the DRM reaction mechanism by applying Density Functional Theory (DFT) calculations. The proposed reaction pathway, which is shown in Figure 6, suggested that the oxidation pathway of CH was more favorable in comparison to that of C.

The morphology dependence of the catalytic properties of Ni/CeO_2 for DRM was investigated by Du et al. [108], who concluded that nanorods displayed more excellent catalytic activity and enhanced anti-coking properties in comparison to nanocubes, owing to the oxygen vacancies and the mobility of lattice oxygen. According to previously published relevant works, the lattice oxygen can transfer to the adjacent nickel particles and then react with CH_x, generating carbon monoxide and hydrogen. Then, CO_2 dissociation, as well as oxygen mobility, can support the supplement of lattice oxygen. These last works underline the key part of lattice oxygen in C–H bond dissociation.

Khalesi et al. [99] conducted a comparative study with the aim of identifying the best alkaline earth metal substitution in La-Ni-Al perovskite oxide. The results showed that the strontium-substituted catalysts outperformed their calcium-substituted counterparts in terms of CH_4 conversion, selectivity, and yields, with $Sr_{0.8}L_{0.2}Ni_{0.3}Al_{0.7}O_{2.6}$ showing the higher value. On the other hand, calcium-substituted catalysts were proved to be more stable in comparison to strontium-substituted samples in the temperature range of 650–800 °C.

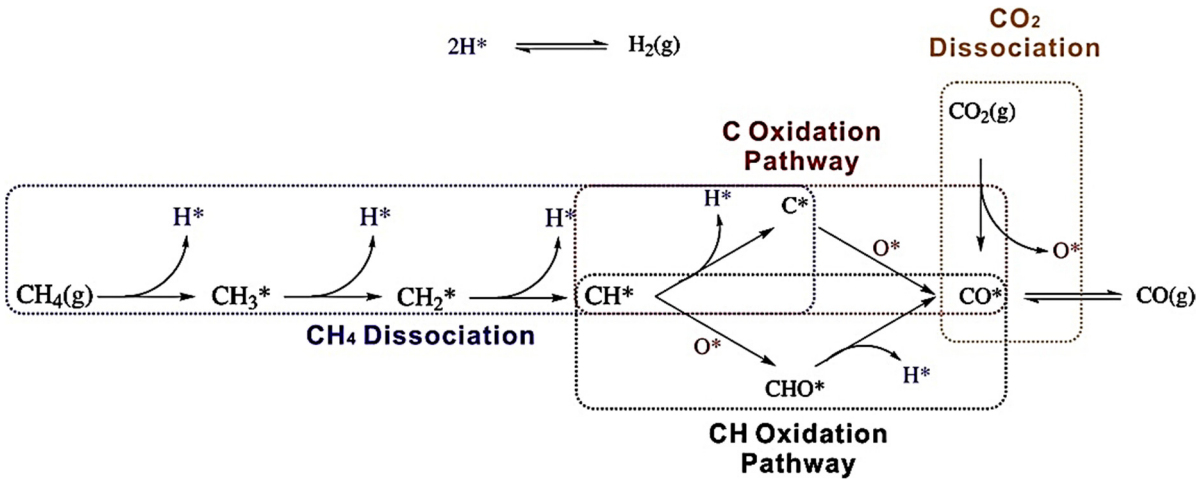


Figure 6. Reaction pathways of DRM proposed by Wang et al. Reproduced with permission from Ref. [50]. Copyright 2014, *Journal of Catalysis*.

3.3. $AB_1B_2O_3$ Perovskite Catalysts

Partial substitution on B-site cations is more difficult in comparison to that of A-site cations. Initially, following catalyst reduction, the addition of reducible metallic elements at the B site would lead to the generation of metal alloy particles. Conversely, considering that the substituting element is inert, the reduction of the catalyst would result in the formation of nickel nanoparticles supported over mixed oxides. Table 2 summarizes the related research.

Table 2. $AB_1B_2O_3$ perovskite catalysts for DRM.

Perovskite	Operating Conditions	CH_4 Conversion Order	Carbon Deposition	Ref.
$LaNiO_3$ $LaNi_{0.8}Zn_{0.2}O_3$ $LaNi_{0.6}Zn_{0.4}O_3$ $LaNi_{0.4}Zn_{0.6}O_3$ $LaNi_{0.2}Zn_{0.8}O_3$ $LaZnO_3$	T = 750 °C WHSV = 180,000 mL g^{-1} h^{-1} CH_4:CO_2:He = 1:1:1	$LaNi_{0.8}Zn_{0.2}O_3$ > $LaNi_{0.6}Zn_{0.4}O_3$ > $LaNiO_3$ > $LaNi_{0.4}Zn_{0.6}O_3$ > $LaNi_{0.2}Zn_{0.8}O_3$ > $LaZnO_3$	0.7%—75 h 0.4%—75 h - - - -	[109]
$LaNiO_3$ $LaNi_{0.9}Ru_{0.1}O_3$ $LaNi_{0.8}Ru_{0.2}O_3$ $La_{3.5}Ru_{4.0}O_3$	T = 750 °C WHSV = 7200 mL mL g^{-1} h^{-1} CH_4:CO_2 = 1:1	$LaNiO_3$ > $LaNi_{0.9}Ru_{0.1}O_3$ > $LaNi_{0.8}Ru_{0.2}O_3$~$La_{3.5}Ru_{4.0}O_3$	65.7%—14 h 20.3%—14 h 6.7%—14 h 0.9%—14 h	[110]
$LaNiO_3$ La_2NiO_4 $La_2Ni_{0.5}Fe_{0.5}O_4$ $LaNi_{0.5}Fe_{0.5}O_3$	T = 750 °C WHSV = 120,000 mL g^{-1} h^{-1} CH_4:CO_2 = 1:1	$LaNiO_3$~La_2NiO_4 > $La_2Ni_{0.5}Fe_{0.5}O_4$ > $LaNi_{0.5}Fe_{0.5}O_3$	31.0%—4 h 18.0%—4 h 3%—4 h 9%—4 h	[111]
$LaNiO_3$ $LaNi_{0.8}Cu_{0.2}O_3$ $LaNi_{0.6}Cu_{0.4}O_3$ $LaNi_{0.4}Cu_{0.6}O_3$ $LaNi_{0.2}Cu_{0.8}O_3$ $LaCuO_3$	T = 750 °C WHSV = 180,000 mL g^{-1} h^{-1} CH_4:CO_2:He = 1:1:1	$LaNiO_3$ > $LaNi_{0.6}Cu_{0.4}O_3$ > $LaNi_{0.4}Cu_{0.6}O_3$ > $LaNi_{0.8}Cu_{0.2}O_3$ > $LaNi_{0.2}Cu_{0.8}O_3$ > $LaCuO_3$	- - - - - -	[112]
La_2NiO_4 $La_2Ni_{0.9}Cu_{0.1}O_4$ $La_2Ni_{0.8}Cu_{0.2}O_4$ $La_2Ni_{0.7}Cu_{0.3}O_4$ $La_2Ni_{0.6}Cu_{0.4}O_4$	T = 750 °C WHSV = 18,000 mL g^{-1} h^{-1} CH_4:CO_2 = 1:1	La_2NiO_4 > $LaNi_{0.9}Cu_{0.1}O_4$ > $LaNi_{0.8}Cu_{0.2}O_4$ > $LaNi_{0.7}Cu_{0.3}O_4$ > $LaNi_{0.6}Cu_{0.4}O_4$	0.4 $g_c g^{-1} h^{-1}$—4 h 0.18 $g_c g^{-1} h^{-1}$—5 h 0.01 $g_c g^{-1} h^{-1}$—5 h 0.01 $g_c g^{-1} h^{-1}$—5 h 0.01 $g_c g^{-1} h^{-1}$—5 h	[113]

Table 2. *Cont.*

Perovskite	Operating Conditions	CH_4 Conversion Order	Carbon Deposition	Ref.
$LaNiO_3$	T = 750 °C GHSV = 15,000 mL g^{-1} h^{-1} CH_4:CO_2:N_2 = 1:1:2	$LaNi_{0.6}Mn_{0.4}O_3$ > $LaNi_{0.4}Mn_{0.6}O_3$ > $LaNi_{0.8}Mn_{0.2}O_3$ > $LaMnO_3$ > $LaNi_{0.2}Mn_{0.8}O_3$ > $LaNiO_3$	-	[114]
$LaNi_{0.8}Mn_{0.2}O_3$			-	
$LaNi_{0.6}Mn_{0.4}O_3$			-	
$LaNi_{0.4}Mn_{0.6}O_3$			-	
$LaNi_{0.2}Mn_{0.8}O_3$			-	
$LaMnO_3$			-	

The literature suggests that the addition of appropriate amounts of zirconium, zinc, and titanium has a promotional effect on the activity and stability (carbon resistance) [115,116]. For example, zinc can serve as a promoter, reinforcing the M-O-La bond, thus preventing the migration of active nickel nanoparticles [109,117]. Dama et al. [118] also used the Ruddlesden–Popper-type perovskite oxide $Sr_{n+1}Ti_{n-x}Ni_xO_{3n+1}$ to investigate syngas production. The results indicated a direct relationship between the order of the Ruddlesden–Popper phase and activity, oxygen vacancies, and metal–support interaction, as the $SrTi_{1-x}Ni_xO_{3-\delta}$ (n = ∞) sample had the highest catalytic activity.

The partial substitution of nickel by ruthenium on B sites to produce bimetallic catalysts has also been examined. Rivas et al. [119] reported that a low degree of ruthenium loading ($LaNi_{0.95}Ru_{0.05}O_3$) can modulate the surface of the catalyst and improve nickel reduction, as well as dispersion. The above results were in contrast to Araujo et al.'s work [110], which reported that Ru-O-La's bond was reinforced by the addition of ruthenium on the B site. Even though the results with respect to catalytic activity were contradictory, they also confirmed the positive effect of the ruthenium addition on the stability of the $LaNi_{0.9}Ru_{0.1}O_3$ and $LaNi_{0.8}Ru_{0.2}O_3$ samples. Yasyerli et al. [120] tested nickel–ruthenium catalysts supported on MCM-41 and varied the amount of ruthenium (i.e., 0.5–3.0 wt%). It was found that the highest catalytic activity was achieved when x = 0.5 wt%. The positive effect of adding small amounts of ruthenium was also discussed by Zhou et al. [121]. The authors observed that increasing the ruthenium loading in Ru-Ni-Mg-O perovskites increased heterogeneity, as RuO_2 was easily segregated and remained undissolved in the NiO-MgO during calcination. That being said, the correlation between adding too much ruthenium and poor catalytic performance is indisputable. However, the contrastive results in terms of catalytic activity need to be further clarified. A possible explanation could be that an excess amount of ruthenium cannot be incorporated into B sites, as it would compromise the synergetic effect between the two metals. Moreover, optimizing the quantity of noble metals such as ruthenium or rhodium to ensure a high catalytic performance is needed owing to the cost limitations.

The addition of Fe (secondary metal to nickel) on B sites producing bimetallic catalyst has been shown to enhance both the catalytic activity and stability. For example, the beneficial effect on the catalytic performance of nickel–iron catalysts used in DRM was corroborated by Wang et al. [122,123], a fact that was ascribed to the generation of uniform nickel–iron alloy particles. Oxide precursors with different structures, such as perovskites, hydrotalcites, and spinels, have been employed to generate these alloy nickel–iron nanoparticles due to the increased oxygen affinity of iron, which endows the catalyst with anti-coking properties [124]. A noteworthy study was conducted by Jahangiri et al. [125], who revealed that $LaNi_xFe_{1-x}O_3$ can have different structures based on the value of x (i.e., x < 0.5 rhombohedral phase, x > 0.5 orthorhombic phase, x = 0.5 both phases). De Lima et al. [117] reported that low amounts of iron added as a secondary metal to nickel in $LaNiO_3$ perovskites improved the catalytic performance with respect to both the catalytic activity and stability. The H_2-TPR tests showed that an increase in iron content caused an increase to the second reduction peak at temperatures higher than 600 °C, corroborating iron's stabilizing effect. The authors also noticed that both nickel and iron are reduced during the second reduction step and transformed into more stable nickel–iron alloys. Provendier et al. [78] also corroborated the alloy formation by carrying out several

characterization techniques. The results of the transmission electron microscopy–energy-dispersive X-ray spectroscopy (TEM-EDS) measurements conducted at different areas of the sample ($LaNi_{0.3}Fe_{0.7}O_3$) demonstrated that the original structure of the fresh perovskite was destroyed under DRM conditions (time-on-stream tests at 800 °C). Figure 7 showcases the differences in lanthanum content between the initial area 1 and areas 2–9, where they were either lanthanum-rich or lanthanum-deficient.

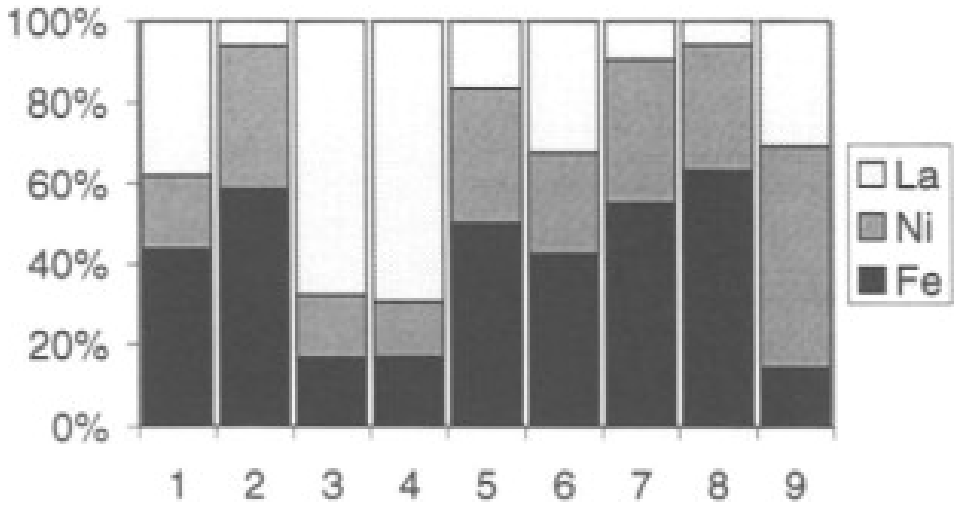


Figure 7. TEM-EDS in different $LaNi_{0.3}FE_{0.7}O_3$ areas, where area 1 corresponds to initial structure composition (200 nm), and areas 2–9 correspond to different areas (14 nm). Reproduced with permission from Ref. [78]. Copyright 1998, *Studies in Surface Science and Catalysis*.

In addition, the EDS analysis in the spent sample showed that the Ni/Fe ratio was almost constant (Figure 8), indicating the formation of a nickel–iron alloy. In addition, the Mossbauer spectroscopic analysis also confirmed the presence of a nickel–iron alloy. In particular, a shift in the hyperfine field was detected, which corresponds to the metallic iron peak in relation to the alpha-iron peak, and this shift varied according to the different iron loadings.

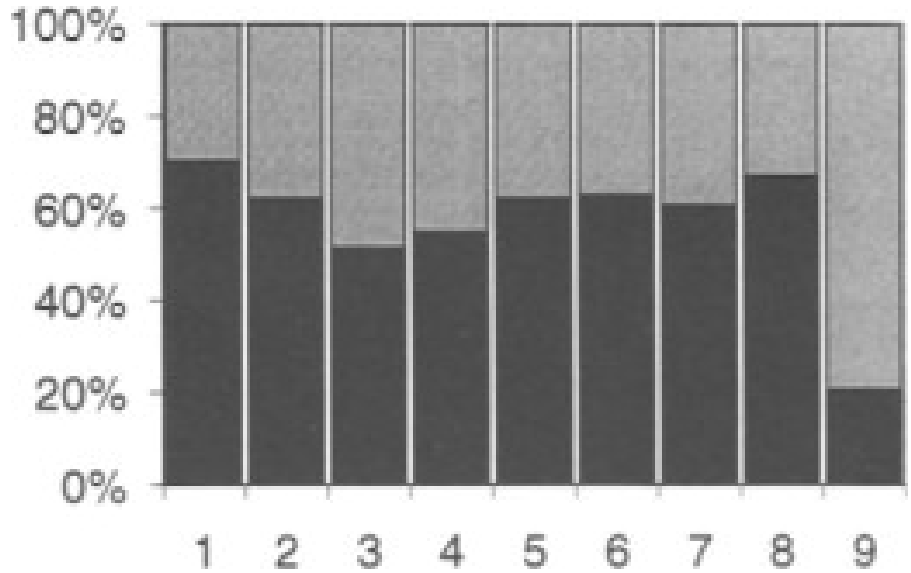


Figure 8. EDS in the spent $LaNi_{0.3}FE_{0.7}O_3$ (light grey: Ni; dark grey: Fe). Reproduced with permission from Ref. [78]. Copyright 1998, *Studies in Surface Science and Catalysis*.

As previously discussed, Fe-substituted perovskites showed increased stability for DRM. Song et al. [111] carried out TPR measurements and showed that the addition of iron into B sites enhanced the stability of the structure and caused an upward change in the reduction temperature, but with a tradeoff on CH_4 conversion. This was consistent with Tomishige's work [126], in which it was reported that nickel–iron alloys can reduce the number of the active nickel surface sites, which were responsible for the dissociation of C–C and C–H bonds, and resultantly compromise the activity. On the other hand, the addition of iron facilitated the adsorption of oxidative species, which were responsible for the suppression of carbon deposition. Theofanidis et al. [127] highlighted the importance of adding the appropriate amount of iron to the Ni-Fe/$MgAlO_4$ catalysts used in DRM. The authors reported improved activity for certain iron amounts added and decreased activity when too much iron was added. An in situ XRD analysis demonstrated that the DRM reaction pathway proceeded via the Mars–van Krevelen mechanism, as presented by the following equations.

$$CH_4 \rightarrow C_{Ni} + 2H_2 \quad (10)$$

$$Fe + xCO_2 \rightarrow FeO_x + xCO \quad (11)$$

$$FeO_x + C_{Ni} \rightarrow xCO + Ni + Fe \quad (12)$$

$$FeO_x + H_2 \rightarrow Fe + H_2O \quad (13)$$

The positive influence of the redox cycle ($Fe^{2+}O/Fe^0$) on resisting carbon deposition was also discussed by Kim et al. [128]. Their results suggested the dynamic nature of the catalyst, which underwent dealloying via oxidation by carbon dioxide and re-alloying via its reduction by carbon species. The originality of this work lies with the fact that a significant phase separation in the catalysts under atmospheres with a high H_2/CO_2 ratio was avoided [128]. Tsoukalou et al. [129] tested the catalytic performance of a reduced $LaNi_{0.8}Fe_{0.2}O_3$ in DRM and reported the deallocation of the initially formed nickel–iron alloy particles and iron oxidation to FeO_x. The presence of FeO_x eventually led to the formation of $LaFeO_3$, which, in turn, encapsulated nickel nanoparticles and compromised the catalytic activity.

Nickel–cobalt bimetallic-supported catalysts ($LaNi_xCo_{1-x}O_3$) have been widely studied for reforming reactions and especially for the reforming of ethanol [130,131]. Valderrama et al. [132] investigated the catalytic behavior of this type of perovskite ($LaNi_xCo_{1-x}O_3$) in DRM. The results indicated increased activity for samples with x bigger than 0.2. It is noted that information regarding the anti-coking ability of the tested catalysts was not provided. Mousavi et al. [133] synthesized $LaNi_{0.5}Co_{0.5}O_3$ perovskites and examined the catalytic performance under the severe DRM conditions. Cobalt partial substitution brought improved carbon resistance; however, the catalytic activity was partly afflicted.

Copper can also be added as a secondary metal to nickel catalysts, generating bimetallic-supported catalysts. When searching through the available literature, one can see that copper-doped samples showed similar catalytic behavior to their cobalt-doped counterparts, meaning that carbon resistance was improved while the catalytic activity dropped [113]. For example, Touahra et al. [134] prepared $LaCu_{0.53}Ni_{0.47}O_3$ and $LaCuO_3$ perovskites via the sol–gel method and 5%NiO/$LaCuO_3$ by using impregnation. The copper-doped sample, as expected, showed increased resistance to coke formation but poor catalytic activity in comparison to $LaCuO_3$ and 5%NiO/$LaCuO_3$. Contrary to the consensus, Moradi et al. [112] synthesized $LaNi_{1-x}Cu_xO_3$ (ternary perovskite oxides) by employing a sol–gel-related method in propionic acid and suggested higher activities and selectivities toward syngas products for the substituted samples. Increasing the amount of added copper generated CuO and La_2CuO_4 phases, in addition to the perovskite phase, which resulted in increasing the mean particle size of the particles involved in DRM.

Valderrama et al. [74] investigated the influence of manganese in $LaNiO_3$ perovskite and reported that low manganese loadings were able to enhance the catalytic performance

of the catalyst in terms of both activity and stability. The addition of manganese led to high dispersion of the reduced nickel on $La_2O_2CO_3$-MnO_x, resulting in the hindrance of carbon deposition. Furthermore, the redox behavior of manganese on Mn-substituted perovskites was similar to that of iron's, meaning that it can impart stability to the perovskite. Wei et al. [135] drew the same conclusions for nickel-substituted $LaMnO_3$ samples. Another interesting work was carried out by Kim et al. [136], who prepared a trimetallic lanthanum–nickel perovskite containing both manganese and cobalt at the B site. Interestingly, the catalyst showed exceptional catalytic behavior, as the addition of manganese induced high catalytic activity, while the addition of cobalt imparted high stability to coke formation.

A recent noteworthy work was carried out by Shahnazi et al. [114], who prepared manganese-substituted $LaNiO_3$ perovskite catalysts ($LaNi_{1-x}Mn_xO_3$) via ultrasonic spray pyrolysis. The addition of manganese to the perovskite matrix increased the pore size and volume, as well as the surface area by 2.11 times. TPR analysis revealed a lower reduction tendency for $LaNi_{1-x}Mn_xO_3$, indicating increased stability. O_2-TPD showed considerably higher oxygen mobility, which is attributed to the addition of manganese (Figure 9).

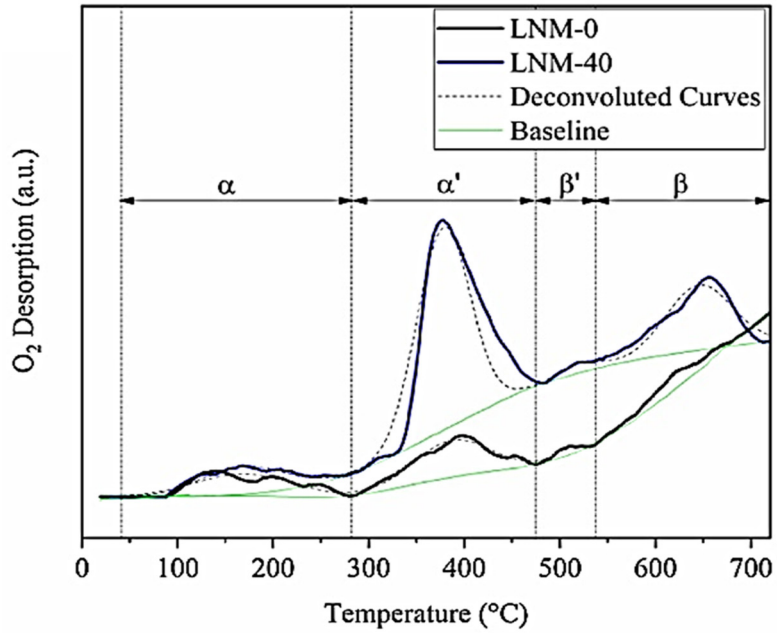


Figure 9. O_2-TPD of fresh $LaNi_{1-x}Mn_xO_3$ (α: surface oxygen species; α′: surface monoatomic oxygen vacancies; β′: perovskite lattice oxygen released from the surface; β: perovskite lattice oxygen desorbed from the bulk). Reproduced with permission from Ref. [114]. Copyright 2021, *Journal of CO_2 Utilization*.

In addition, partial manganese substitution improved the catalytic behavior of the catalyst in terms of both activity and stability, with $LaNi_{0.6}Mn_{0.4}O_3$ achieving the better performance. It was also reported that the presence of manganese suppressed coke formation, and amorphous carbon was formed instead of whiskers. The XPS results indicated that the presence of amorphous carbon was assigned to the reversible transformation of Mn^{4+} and Mn^{3+}, leading to increased oxygen mobility. Higher resistance to sintering for $LaNi_{1-x}Mn_xO_3$ compared to bulk $LaNiO_3$ was also corroborated by the microstructural characterization of the used samples. The results showed that the catalytic mechanisms were significantly affected by the addition of manganese, where the formation of $La_2O_2CO_3$ intermediate aided $LaNiO_3$ in removing carbon. On the other hand, the stable $LaNi_{1-x}Mn_xO_3$, which had a high oxygen capacity and mobility, removed coke through a cyclic redox mechanism.

3.4. $A_1A_2B_1B_2O_3$ Perovskite Catalysts

Numerous works have been carried out with a view to investigate the effect of the substitution of both A and B sites on catalytic activity and stability, with the majority of these studies trying to optimize the stoichiometry in order to achieve improved catalytic behavior. Valderrama et al. [137] focused on optimizing $La_xSr_{1-x}Ni_yCo_{1-y}O_3$ perovskite. The authors reported improved activity and resistance toward coke for the sample under consideration. High carbon resistance was attributed to the $SrCO_3$ intermediary phase, which promoted the formation of $La_2O_2CO_3$ and SrO regeneration phases that, in turn, could serve as inhibitors against carbon deposition.

Sutthiumporn et al. [138] studied the DRM over $La_{0.8}Sr_{0.2}Ni_{0.8}X_{0.2}O_3$ (X = Fe, Cu, Cr, Co, and Bi) prepared via the sol–gel method and tried to shed light on the effect of lattice oxygen on both carbon resistance and C–H activation. The results showed higher methane conversion for the cobalt- and copper-doped samples at the initial stage. Nevertheless, the copper-doped ($La_{0.8}Sr_{0.2}Ni_{0.8}Cu_{0.2}O_3$) perovskite exhibited poor carbon resistance due to particle agglomeration. On the other hand, even though $La_{0.8}Sr_{0.2}Ni_{0.8}Fe_{0.2}O_3$ perovskite was not that active initially, it was considerably stable, a fact that was confirmed by a Thermogravimetric Analysis (TGA) analysis, with negligible amounts of carbon detected. The XPS results suggested higher oxygen lattice mobility over the copper-doped sample ($La_{0.8}Sr_{0.2}Ni_{0.8}Cu_{0.2}O_3$) in comparison to that of the iron-doped one ($La_{0.8}Sr_{0.2}Ni_{0.8}Fe_{0.2}O_3$). Moreover, the methane-TPR analysis showed that iron-doped ($La_{0.8}Sr_{0.2}Ni_{0.8}Fe_{0.2}O_3$) perovskite outperformed copper-doped ($La_{0.8}Sr_{0.2}Ni_{0.8}Cu_{0.2}O_3$) perovskite in terms of initial methane activation, presumably because of mobile lattice oxygen species, which activated the C–H bond. Furthermore, the addition of iron seemed to improve the metal–support interaction, which consequently enhanced carbon suppression.

In summary, A-site substitution is usually correlated with the oxygen vacancy formation, which is generally considered to be beneficial to enhance carbon resistance. On the other hand, B-site substitution with reducible metals often results in a synergetic effect, which can be either beneficial or detrimental. However, the mechanism of partial substitution of both the A and B sites and its subsequent effect on DRM have yet to be fully clarified, and further research would help address the issue.

3.5. Mesoporous/Supported Perovskite Catalysts

A significant limitation regarding the perovskite catalysts is the absence of micropores and surface area ($\geq$10 m^2 g^{-1}), a problem that cannot be solved by partial substitution of the A or B site. A small surface area, along with weak mechanical strength, seems to prevent perovskite oxide catalysts from commercialization. Nowadays, different techniques that depend on morphology modulation have been adopted to address this issue.

The surface area could be increased by decreasing the particle size of the perovskite catalysts. A typical method to achieve this is by dispersing perovskite onto a support such as alumina, mesoporous silica, etc., which are known for their high surface area [139–141]. Therefore, this type of supported perovskite catalyst, which is usually prepared using the impregnation method (i.e., support is inserted into the mixture of precursor solution) to accurately control the perovskite loading, exhibits strong metal–support interaction and the ability to produce highly dispersed nanosized particles on the support [71].

Yadav et al. [141] prepared $LaNi_xFe_{1-x}O_3$ perovskites supported on different supports (i.e., SiO_2, Al_2O_3, and MgO) and tested their performance in DRM. Firstly, it was reported that SiO_2 support led to higher dispersion and improved conversions due to the increased number of active sites compared to Al_2O_3 and MgO support. Next, the authors observed that 40 wt% $LaNi_{0.75}Fe_{0.25}O_3$ supported on silica outperformed, in terms of catalytic activity and stability, the bulk perovskite-derived counterparts. In this regard, the XRD analysis showed that the peaks of the individual perovskite oxide phases were insignificant in the supported samples, indicating high dispersion. Nevertheless, the formation of silicate species was noticed at higher loadings (Figure 10). The FTIR analysis corroborated the existence of silicate species accommodated on the periphery of the samples, though without

affecting the selectivity or conversions. This denotes the inability of silicate phase to encapsulate the nickel nanoparticles on the surface. Similarly, Sellam et al. [63] investigated $LaNiO_3/SiO_2$-supported catalysts and reported an improved catalytic performance owing to the higher surface area and nanosized nickel particles.

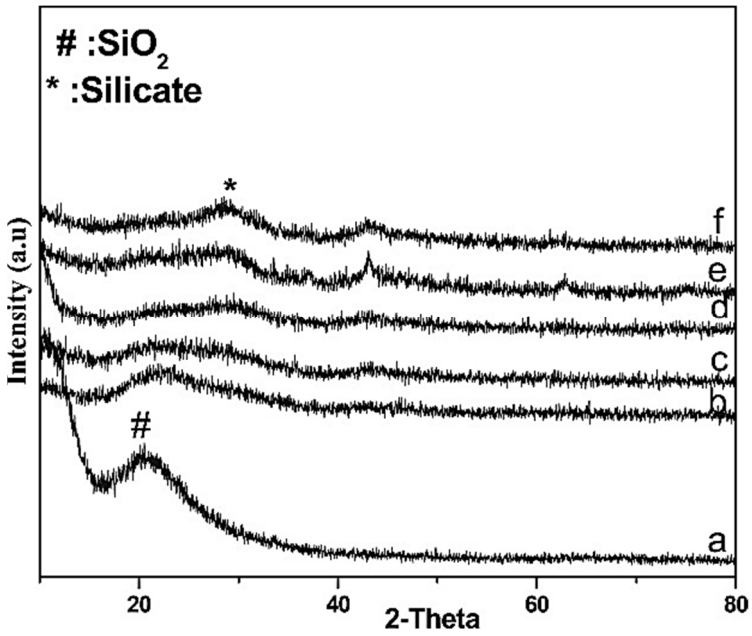


Figure 10. XRD peaks of $ZLaNi_{0.75}Fe_{0.25}O_3/SiO_2$ with different $LaNi_{0.75}Fe_{0.25}O_3$ loadings in the support. (**a**) SiO_2, (**b**) $10LaNi_{0.75}Fe_{0.25}O_3/SiO_2$, (**c**) $20LaNi_{0.75}Fe_{0.25}O_3/SiO_2$, (**d**) $30LaNi_{0.75}Fe_{0.25}O_3/SiO_2$, (**e**) $40LaNi_{0.75}Fe_{0.25}O_3/SiO_2$, and (**f**) $50LaNi_{0.75}Fe_{0.25}O_3/SiO_2$ were calcined at 973 K for 1 h. Where, Z = 10, 20, 30, 40, and 50; and x = 0, 0.25, 0.5, 0.75, and 1. Reproduced with permission from Ref. [141]. Copyright 2019, *International Journal of Hydrogen Energy*.

Zhang et al. [142] prepared $LaNiO_3$ perovskites supported on mesoporous silica and tried to capitalize the confinement effect derived from the use of this mesoporous material. It is known that the catalyst precursor can be confined with a layer of mesoporous barrier to produce more stable nickel particles and, thus, avoid sintering and carbon deposition. That being said, the authors used $LaNiO_3$ nanocubes embedded in SiO_2 for the DRM, as shown in Figure 11. The $Ni/La_2O_3@SiO_2$ obtained upon the hydrogen pretreatment was able to both support and confine nickel nanoparticles, resulting in enhanced anti-coking properties.

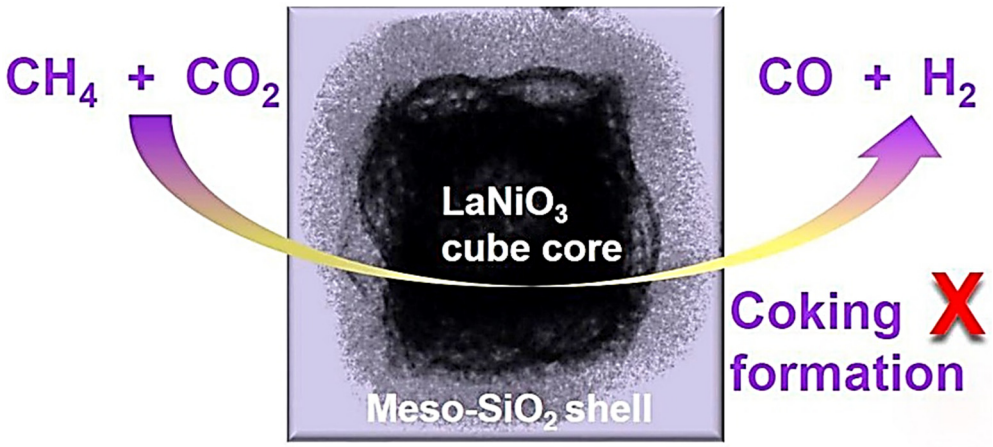


Figure 11. $Ni/La_2O_3@SiO_2$ scheme for DRM. Reproduced with permission from Ref. [142]. Copyright 2018, *Microporous and Mesoporous Materials*.

Wang et al. [143] synthesized $LaNiO_3$ perovskites supported on SiO_2, SBA-15, and MCM-41 carriers and investigated the influence of pore topology on their catalytic performance. As shown in Figure 12, isotherms of the supported samples are less steep and vertical in comparison to the those of their carriers. In addition, the slightly lower values of P/P_0 suggested the incorporation of perovskite particles into the mesopores of the carries. With respect to the narrow pore size distributions, SiO_2 showed higher values in comparison to those of two other carriers (i.e., SBA-15 and MCM-41). Moreover, $LaNiO_3$/MCM-41 showed the highest activity, followed by $LaNiO_3$/SBA-15 and $LaNiO_3/SiO_2$. However, time-on-stream tests at 700 °C for 60 h revealed that $LaNiO_3$/SBA-15 was more stable than $LaNiO_3$/MCM-41. From the TPR results (Figure 13), it can be seen that a higher reduction temperature peak was shifted to higher temperatures in $LaNiO_3$/MCM-41 and $LaNiO_3$/SBA-15 catalysts, suggesting strong metal–support interaction and, thus, improved stability. The authors also reported the co-occurrence of an RWGS reaction since the ratio of H_2/CO was less than unity.

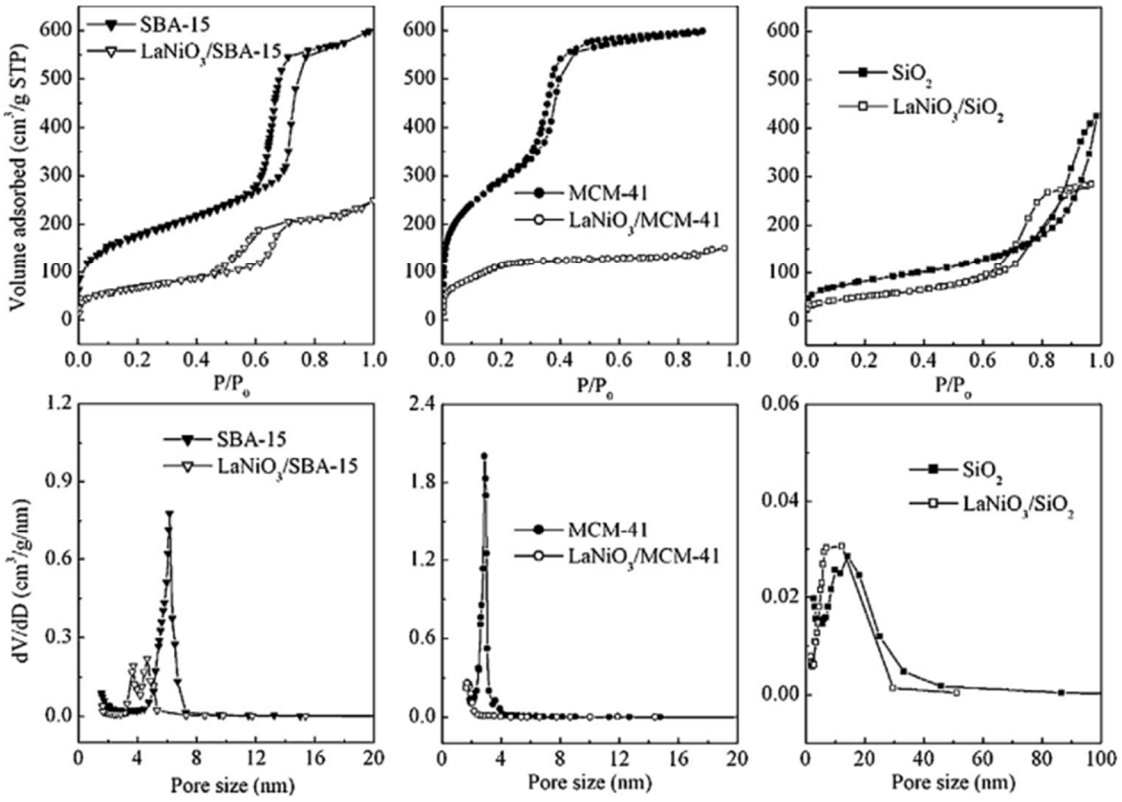


Figure 12. Nitrogen adsorption isotherms and pore size distributions of mesoporous $LaNiO_3$ and its supports. Reproduced with permission from Ref. [143]. Copyright 2013, *Catalysis Today*.

Rivas et al. [144] prepared $LaNiO_3$, $La_{0.8}Ca_{0.2}NiO_3$, and $La_{0.8}Ca_{0.2}Ni_{0.6}Co_{0.4}O_3$ as catalyst precursors that were both bulk and supported on an SBA-15 carrier and tested them in DRM. The results showed better catalytic behavior for the supported catalysts. Moreover, the authors reported that, apart from the previously mentioned confinement effect, there was the dilution effect exerted by the mesoporous catalyst, which limited the heat diffusion issues associated with DRM's high endothermicity.

A noteworthy work was conducted by Nair et al. [145], who synthesized mesoporous $LaNiO_3$ perovskite by using SBA-15 as a hard template for DRM. Following the removal of the SBA-15 template, ordered structures resembling nanowires were obtained. The Brunauer–Emmett–Teller (BET) analysis that was performed showed an increased surface area for the nanocast $LaNiO_3$ (150 $m^2\ g^{-1}$) compared to that of the bulk $LaNiO_3$ (10 $m^2\ g^{-1}$). The reducibility of the bulk and nanocast $LaNiO_3$ was monitored by carrying out H_2-TPR.

It was reported that both samples had similar reduction profiles; however, no shoulder was apparent for the nanocast $LaNiO_3$, as result that can be attributed to the lack of grain boundaries in the nanocast samples (Figure 14). The peak position of the second reduction step indicated that the complete reduction of the nanocast $LaNiO_3$ occurred at a barely lower temperature compared to that used for the bulk $LaNiO_3$. In addition, the XRD pattern of the reduced perovskites (Figure 15) showed the total destruction of the perovskite structure at temperatures below 700 °C (black and blue curves) for both bulk and nanocast $LaNiO_3$, resulting in the formation of highly dispersed nickel in La_2O_3. The results from the catalytic tests revealed increased catalytic activity presumably due to the higher surface area and volume pore that provided more nickel active sites that were accessible to CO_2 and CH_4.

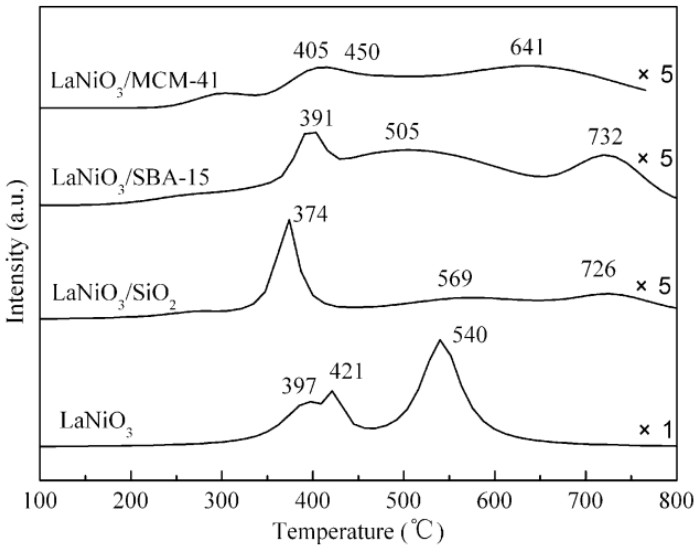


Figure 13. TPR profiles of bulk and supported $LaNiO_3$ perovskites. Reproduced with permission from Ref. [143]. Copyright 2013, *Catalysis Today*.

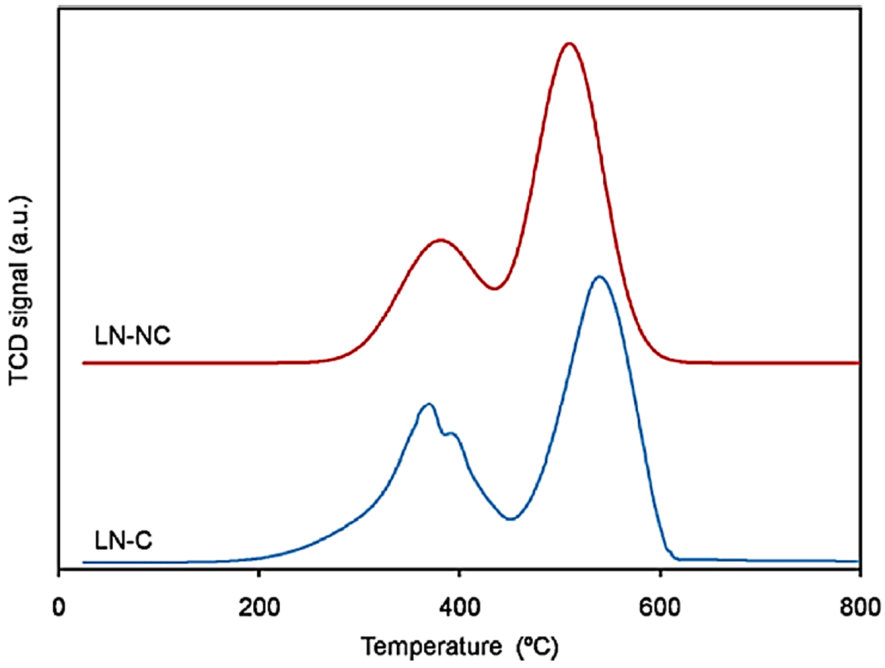


Figure 14. H_2-TPR profiles of nanocast (red) and bulk (blue) $LaNiO_3$. Reproduced with permission from Ref. [145]. Copyright 2014, *ACS Catalysis*.

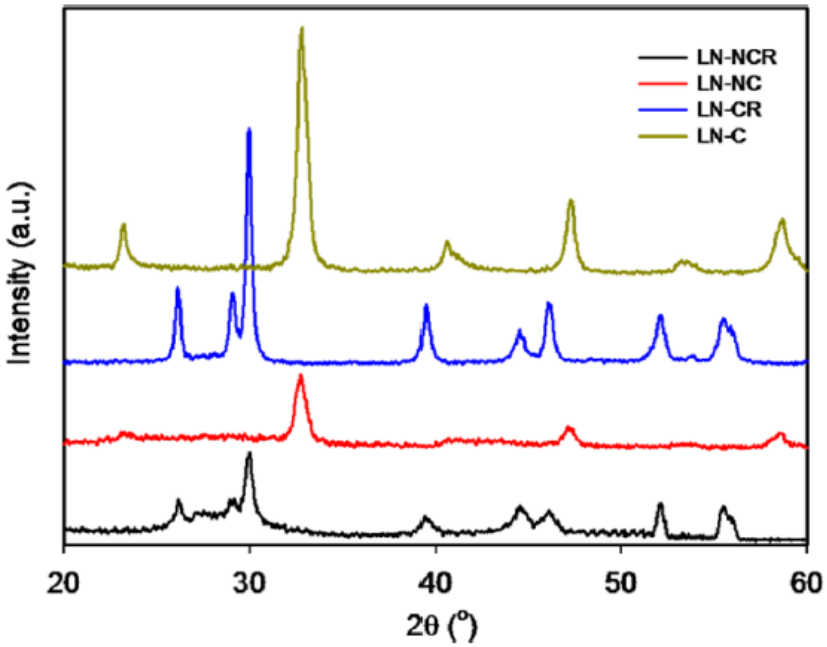


Figure 15. XRD pattern of $LaNiO_3$ and reduced at 700 °C Ni/La_2O_3. Reproduced with permission from Ref. [145]. Copyright 2014, *ACS Catalysis*.

A similar technique to prepare mesoporous $LaNiO_3$/SBA-15 catalysts was adopted by Duan et al. [146] but for the reaction of the partial oxidation of methane.

In a recent study, Ruan et al. [147] prepared a $LaAl_{0.25}Ni_{0.75}O_3$ perovskite catalyst by using SBA-15 as a hard template for DRM. The results from different characterization techniques (i.e., H_2-TPR, CO_2-TPD, FT-IR, TEM-EDS, and XRD) revealed that the strong metal–support interaction, larger surface area, and increased number of strong basic sites of $LaAl_{0.25}Ni_{0.75}O_3$/SBA-15 were due to the unique structural characteristics of the catalyst, as well as the addition of proper amounts of silica. The authors also reported that the $LaAl_{0.25}Ni_{0.75}O_3$/SBA-15 catalyst outperformed, in terms of both activity and stability, the catalyst using commercial silica with a specific irregular channel structure and the bulk $LaAl_{0.25}Ni_{0.75}O_3$ catalyst. Following a 36-hour-long stability test, a conversion of more than 75% was maintained for the reactants (GSHX = 192,000 mL h^{-1}).

Rabelo-Neto et al. [10] used $CeSiO_2$ and Al_2O_3 basic oxides as carriers for $LaNiO_3$. The formation of Ce–O–Si bonds, which were produced via the introduction of Si to CeO_2, aided in the catalyst's resistance to sintering and increase in surface area. The TPR results showed an increase in the reduction temperature for the supported $LaNiO_3/CeSiO_2$ catalyst compared to the bulk $LaNiO_3$, thus indicating a strong metal–support interaction. Along with the increased anti-coking ability brought in by the strong metal–support interaction, the redox behavior of ceria oxide (Ce^{+4}/Ce^{3+}) instigated high oxygen mobility, thus assisting in the oxidization of carbon residues. Massaoudi et al. [148] carried out a study on supported $La_xNiO_y/MgAl_2O_4$ and bulk $LaNiO_3$ perovskites in DRM. The H_2-TPR analysis showed that the supported samples were less reducible than the bulk ones, owing to the formation of $NiAl_2O_4$ during the calcination. Typically, the presence of $NiAl_2O_4$ improves the nickel dispersion over the support surface [148], which explains the enhanced catalytic performance of the supported $La_xNiO_y/MgAl_2O_4$ catalysts.

Yadav et al. [141] prepared and tested, in the DRM, perovskite catalysts (Ni 75wt% and Zr-Ce 25wt%, changing the ratio) supported on silica (SiO_2) and focused on the influence of alumina and magnesia on the support. The results showed that the introduction of a certain amount of ceria (x = 0.05) aided in increasing the surface area of the catalyst; however, the surface area was almost unchangeable after the SiO_2 was modified with magnesia and alumina. However, the modification of SiO_2 support with alumina and magnesia assisted in enhancing the basicity of the surface of SiO_2 and improving the reactant conversions. On

the other hand, excess amounts of ceria and/or zirconia prevented the perovskite structure formation and led to the production of segregated phases of CeO_2, NiO, and La_2O_3 in the SiO_2-supported sample. The increased H_2/CO ratio that was observed (>1) can be attributed to the dominance of the methane-cracking reaction, which eventually led to coke formation in all catalysts. The authors postulated that the $40LaNi_{0.75}Ce_{0.05}Zr_{0.20}O_3/8MgO$-$SiO_2$ sample exhibited the higher catalytic activity.

3.6. Three-Dimensionally Ordered (3DOM) Macroporous Perovskites

Furthermore, 3DOM perovskite materials have attracted global attention owing to their flexibility, tailorability, high stability, and unique macroporous structure that facilitates diffusion toward the active sites [149]. Typically, 3DOM perovskite-type oxides are prepared using colloidal crystal templates (e.g., polystyrene, poly (methyl-methacrylate), or silica), which are commercial products of high availability [150–152]. At the outset, the synthesis of macroporous perovskites is considered much more feasible compared to that of mesoporous perovskites since they are commercial products with low costs and are available in a variety of sizes, making them adaptable to demand. On the other hand, mesoporous silica has limited availability. Secondly, the synthesis of macroporous perovskites is more environmentally friendly compared to that of mesoporous silica, as harmful chemicals such as NaOH are required to dissolve the silica [146]. Thus far, this group of materials has been reported on works regarding the methane combustion; however, they have yet to be applied in DRM. Non-noble nickel-based catalysts with a 3DOM structure, such as $La_2NiB'O_6$, could be fabricated and tested for DRM in the near future.

4. Kinetic and Mechanistic Considerations

Several mechanisms have been proposed that rely on the type of the catalyst employed for this reaction [113,153]. Typically, CO_2 activation energy is lower than CH_4 activation energy due to the fact that methane has higher stability. A dual active-site mechanism has been proposed for $LaNiO_3$ perovskites used in the DRM. According to this mechanism, CH_4 is decomposed at site X_1, while CO_2 is activated at site X_2. La_2O_3, which is formed after the reduction of $LaNiO_3$ perovskite ($LaNiO_3 \rightarrow$ reduction $\rightarrow Ni/La_2O_3$), can readily react with CO_2 to produce a stable phase of $La_2O_2CO_3$ (Equation (16)), as corroborated by FTIR and XRD analysis [82]. Generally, supports with higher basicity, such as La_2O_3, can promote the chemisorption of CO_2 to produce $La_2O_2CO_3$, which, in turn, has a positive effect on the activation of CH_4 on the active sites [154].

Tsipouriari et al. [155,156] confirmed the formation of $La_2O_2CO_3$, which was involved in CO formation, acting as an oxygen generator during the DRM reaction (Equation (17)).

This group proposed the following widely accepted kinetic mechanism for the DRM reaction over Ni/La_2O_3 catalysts, where RDS (Equations (15), (17), (24) and (26)) denotes the rate-determining step.

$$CH_4 + Ni \leftrightarrow Ni - CH_4,\ K_1\ (\text{equilibrium}) \quad (14)$$

$$Ni - CH_4 \rightarrow Ni - C + 2H_2,\ k_2\ (\text{RDS}) \quad (15)$$

$$CO_2 + La_2O_3 \leftrightarrow La_2O_2CO_3,\ K_3\ (\text{equilibrium}) \quad (16)$$

$$La_2O_2CO_3 + Ni - C \rightarrow La_2O_3 + 2CO + Ni,\ k_4\ (\text{RDS}) \quad (17)$$

$$H_2 + 2 - Ni \leftrightarrow 2H - Ni,\ (\text{equilibrium}) \quad (18)$$

The concurrent occurrence of RWGS includes the following reaction steps:

$$CO_2 + Ni \leftrightarrow Ni - CO_2,\ (\text{equilibrium}) \quad (19)$$

$$Ni - CO_2 + H - Ni \rightarrow Ni - CO + OH - Ni,\ \text{slow} \quad (20)$$

$$OH - Ni + H - Ni \leftrightarrow 2Ni - H_2O, \text{ (equilibrium)} \quad (21)$$

In this regard, the group proposed the following rate expression for the CH_4 consumption:

$$r_{CH_4} = \frac{K_1 k_2 K_3 k_4 p_{CH_4} p_{CO_2}}{K_1 K_3 k_4 p_{CH_4} p_{CO_2} + K_1 k_2 p_{CH_4} + K_3 k_4 p_{CO_2}}, \text{ Model 1} \quad (22)$$

where K_1 represents the adsorption equilibrium constant of methane, k_2 is the rate constant of the surface reaction (methane cracking), K_3 corresponds to the adsorption equilibrium of the carbonatation reaction, and k_4 is the rate constant of the reaction between the carbon (carbon deposition) and oxycarbonate species.

Gallego et al. [82,83] proposed a similar equally widespread dual-site reaction mechanism for $LaNiO_3$ and $LaNiO_4$ perovskite catalysts that is shown below. Interestingly, the authors mentioned that the non-reduced perovskite oxide can improve the resistance to coke formation.

$$CH_4 + X_1 \leftrightarrow X_1 - CH_4, \ K_1 \text{ (equilibrium)} \quad (23)$$

$$X_1 - CH_4 \rightarrow X_1 - C + 2H_2, \ k_2 \text{ (RDS)} \quad (24)$$

$$CO_2 + X_2 \leftrightarrow X_2-, \ K_3 \text{ (equilibrium)} \quad (25)$$

$$X_1 - CH_4 + X_2 - CO_2 \rightarrow X_2 + 2CO + X_1, \ k_4 \text{ (RDS)} \quad (26)$$

where X_1 corresponds to the nickel active sites (Ni^0) and X_2 represents the La_2O_3 supports as the active site. On this basis, the following rate expression for the CH_4 consumption was assumed:

$$r_{CH_4} = \frac{K_1 k_2 K_3 k_4 p_{CH_4} p_{CO_2}}{K_3 k_4 p_{CO_2} + K_1 K_3 k_4 p_{CH_4} p_{CO_2} + K_1 k_2 p_{CH_4} + K_1 k_2 K_3 p_{CO_2}}, \text{Model 2} \quad (27)$$

Moradi et al. [157] carried out kinetic studies on the CO_2 reforming of CH_4 over La–Ni-based perovskite and found that the kinetic profile of $LaNiO_3$ resembled that of Ni/La_2O_3.

Table 3 summarizes and compares the calculated kinetic rate parameters found in the literature.

Table 3. Overview of kinetic rate parameters for DRM.

Kinetic Parameters	Temperature Range (°C)	Ref.
Ni/La_2O_3 K_1 $k_2 = 2.61 \times 10^{-3}\exp(-4300/T)$ [mol g^{-1} s^{-1}] $K_3 = 5.17 \times 10^{-5}\exp(8700/T)$ [kPa^{-1}] $k_4 = 5.35 \times 10^{-1}\exp(-7500/T)$ [mol g^{-1} s^{-1}]	650–750	[155]
Ni/La_2O_3 derived from $LaNiO_3$, at T = 700 °C $K_1 = 141 \times 10^{-3}$ [kPa] $k_2 = 0.22326 \times 10^{-3}$ [mol g^{-1} s^{-1}] $K_3 = 15.98 \times 10^{-3}$ [kPa] $K_4 = 13.22 \times 10^{-3}$ [mol g^{-1} s^{-1}]	500–700	[82]
$LaNiO_3$ $K_1 = 279.55\exp(-7502.5/T)$ [kPa^{-1}] $k_2 = 12.27\exp(-10{,}219.2/T)$ [mol g^{-1} s^{-1}] K_3 $k_4 = 0.034\exp(-6968.2/T)$ [kPa^{-1} mol g^{-1} s^{-1}]	650–750	[157]

When searching through the available literature, it can be deduced that most of the reaction mechanisms proposed for DRM follow the Langmuir–Hinshelwood–Hougen–Watson (LHHW) formalism.

Batiot-Dupeyrat et al. [79] corroborated the presence of $La_2O_2CO_3$ hexagonal phase by XRD analysis on the spent samples and indicated that the concurrent realization of nickel reduction with oxycarbonate formation is crucial to limit the effect of RWGS and keep the ratio of H_2/CO close to unity. It was interesting that the catalytic activity improved when the reactants were added at ambient temperature compared to the case in which they were introduced at higher temperatures. This enhanced activity can be attributed to the production of oxycarbonate species, which promoted the CH_4 activation on nickel active sites. Slagtern et al. [154] also denoted the suppressive effect of lanthanum carbonate on coke accumulation, which eventually results in catalyst deactivation. In a recent study, Singh et al. [91] studied the relationship between the solid-phase crystallization and the shape of $LaNiO_3$. The results from 100-hour-long stability tests suggested decreased stability due to coke accumulation for the catalysts developed from $LaNiO_3$ cubes compared to the ones that were derived from rods and spheres whose catalytic stability was unaffected. The remarkable stability of the rod-derived $LaNiO_3$ catalyst can be attributed to both the smaller size and number of nickel nanoparticles in the structure. The results from a more recent study carried out by the same group suggested that solid-phase crystallization defects may be considered a possible cause for the high stability observed [158]. In general, many groups associated the anti-coking ability of the catalyst with the production of carbonate species during the DRM. Nevertheless, Dama et al. [96] proposed a mechanism in which hydroxyl species were involved in the mechanism. Considering these proposed mechanisms, Bhattar et al. [36], in their excellent review, presented the following sequence of reactions for CH_4 and CO_2:

CH_4 activation:

$$CH_4(g) + (5 - x)X \rightarrow CH_x - X + (4 - x)[H - X] \quad (28)$$

$$2[H - X] \leftrightarrow H_2 + 2X \quad (29)$$

$$OH - S \leftrightarrow OH - X \quad (30)$$

$$OH - X + X \leftrightarrow O - X + H - X \quad (31)$$

$$H - X + OH - X \leftrightarrow H_2O(g) + 2X \quad (32)$$

$$CH_x - X + O - X \leftrightarrow CO - X + x[H - X] \quad (33)$$

$$CO - X \leftrightarrow CO(g) + X \quad (34)$$

$$2CO - X \leftrightarrow C(s) + CO_2 + 2X \quad (35)$$

CO_2 activation:

$$CO_2(g) + S \leftrightarrow CO_2 - S \quad (36)$$

$$CO_2 - S + O^{-2} \leftrightarrow CO_3^{-2} - S \quad (37)$$

$$CO_2 - S + OH^- - S \leftrightarrow HCO_3^- - S \quad (38)$$

$$CO_3^{-2} - S + 2(H - S) \leftrightarrow HCO_2^- - S + OH^- - S \quad (39)$$

$$HCO_3^- - S + 2(H - S) \leftrightarrow HCO_2^- - S + H_2O - S \quad (40)$$

$$HCO_2^- - S \leftrightarrow CO - S + OH - S \quad (41)$$

$$CO - S \leftrightarrow CO(g) + S \quad (42)$$

$$2[H-X] \leftrightarrow 2[H-S] \quad (43)$$

Equations (28) and (35) contribute to the coke formation on the catalyst's surface, while Equation (43) refers to the hydrogen atoms spilled over to the support, following methane decomposition [96]. Through this process, hydroxyl groups are produced in strong basic sites. In the previous equations, X represents the metal active site, while S corresponds to the active site of the support. However, specific criteria need to be met so that the above equations can be meaningful and valid, such as the following [157,159–161]:

(1) Perovskite undergoes reduction (active metal should be reduced),
(2) Perovskite is supported on basic oxide,
(3) Rate of carbon dioxide dissociation is inconsiderable in comparison to that of methane,
(4) Negligible surface coverage of hydrogen and carbon monoxide,
(5) A part of active metal is carbon-free under DRM conditions.

The determination of mechanisms for $LaNiO_3$ perovskites used in the DRM has recently gained added impetus via in situ microscopy and spectroscopy studies that can provide evidence for activity–structure correlations. Thus, these techniques can contribute inter alia to a more comprehensive understanding of how oxygen defects influence catalytic behavior during DRM and illuminate their significance as active sites, as well as elucidate their influence on catalytic performance [162–164].

Nezhad et al. [162] carried out in situ synchrotron-based PXRD tests in both DRM mixtures, as well as under pure H_2. The results showed the formation of the perovskite-related counterpart of $LaNiO_3$ (i.e., La_2NiO_4) during the reaction, but this was not the case under pure H_2. The authors also reported the formation of oxygen-deficient structures and transient-related perovskite structures when subjected to heat in the DRM mixture.

Bonmassar et al. [61] employed quantitative in situ X-ray diffraction to uncover the dynamic structural changes taking place in $LaNiO_3$ perovskites during the DRM reaction. The results suggested structure–activity correlations, revealing monoclinic $LaNiO_{2.5}$ and transient oxygen-deficient triclinic $LaNiO_{2.7}$ phases, as well as transformations from the rhombohedral to cubic $LaNiO_3$ structure. The authors also discussed the association of these transitions with the increased DMR activity, which is likely attributed to surface-near nickel exsolution (not detectable by PXRD initially). The formation of the La_2NiO_4 phase was also reported [162] alongside the decomposition of monoclinic $LaNiO_{2.5}$, also affecting the catalytic activity. In addition, a substantial enhancement of DRM activity was observed once the lattice oxygen release from phase transformations toward $Ni^0/La_2O_2CO_3$ was completed, probably owing to the full conversion of the Ni surface to its metallic state that was facilitated by monoclinic $La_2O_2CO_3$. Further transformations resulted in hexagonal La_2O_3, as well as hexagonal $La_2O_2CO_3$, formation for temperatures above 750 °C. This direct activity–structure correlation displayed that the active phase in DRM comprises a mixture of metallic Ni in contact with monoclinic $La_2O_2CO_3$ that acts as a stabilizer for the metallic Ni particles (similar behavior to the CO_2-activated spaces). Notably, the temperatures at which $La_2O_2CO_3$ formation and decomposition occurred were in line with those found in earlier studies of La_2O_3 with pure CO_2. A crystalline La_2O_3 phase at temperatures below 750 °C was not detected, whilst a sequence of reaction steps could not be ruled out [163].

5. Conclusions

The work presented herein provides information regarding the recent advances in the field of La–Ni-based perovskite-derived catalysts used in DRM. The main conclusions are summarized below:

- $LaNiO_3$ gained considerable attention due to the high affinity between CO_2 and La_2O_3, which results in $La_2O_2CO_3$ formation, as well as the strong metal–support interaction provided. The presence of $La_2O_2CO_3$ plays a key role in the catalyst's stability, as it can actively react with coke and act as an inhibitor against carbon accumulation on the nickel's surface.

- A-site partial substitutions with alkaline earth or rare earth metals into the perovskite matrix can both induce oxygen vacancies and modify the basicity of the surface of the catalyst, thereby improving coke resistance. The increased amount of lattice oxygen can also promote C–H activation, increase nickel dispersion, and increase the reducibility of the catalyst. Furthermore, redox chemistry of rare earth metals such as Sm, Pr, and Ce has a positive influence on the stability of the catalyst due to the fact that more oxygen for carbon removal is supplied.
- B-site substitution can be reflected in two aspects. Non-reducible metals such as zirconium, and titanium can modify the structure and enhance the metal–support interaction, thus suppressing carbon deposition. On the other hand, reducible metals such as Fe, Co, Ru, and Cu can provide a synergetic effect which can be either beneficial or detrimental. To illustrate this point, the addition of iron generates a nickel-containing alloy which improves the stability of the perovskite. Moreover, the redox chemistry of the iron induces oxygen for coke removal due to the dynamic profile of the catalyst, which undergoes dealloying via oxidation by carbon dioxide and re-alloying via its reduction by carbon species. A smaller nickel particle size and decreased reducibility are related to the addition of iron or cobalt. In addition, cobalt can serve as a promoter owing to its high oxygen affinity, which aids in carbon gasification. Certain amounts of copper and manganese can also improve the catalytic behavior of the perovskite oxides in terms of both activity and stability.
- The preparation of perovskites requires considerably high calcination temperatures to produce materials with considerably small surface areas, thus affecting their catalytic behavior. One method to overcome this problem is to disperse perovskite on certain supports, such as SBA-15 and MCM-41, leading to smaller perovskite particles. Another method is to synthesize porous perovskite catalysts by using templating methods.

However, there are many issues regarding this group of materials that still need to be addressed in order to consider them to be appropriate and effective for industrial DRM applications. Further research is necessary to come up with a better understanding of the thermal stability and coke formation of perovskites. For example, even though perovskites are known for their thermal stability, their structure can irreversibly decompose under extreme DRM conditions. However, the regeneration of the perovskite via multiple TPR-TPO cycles has been reported by a few studies, also resulting in increasing nickel dispersion. From an industrial perspective, the regeneration of the catalyst is a matter of great concern, as is the improvement of the catalytic activity at the industrially desired high WHSV/GHSV.

As was previously mentioned, the addition of reducible metal on B-sites can be either beneficial or detrimental. It has not been established yet whether a core–shell-like structure or uniform alloy is formed between the two metals that is clearly associated with their catalytic performance.

DFT calculations could be a powerful tool for designing perovskite catalysts, as it allows us to predict crucial properties, such as lattice oxygen mobility, which could aid in finding the best stoichiometry without educated guesses.

Finally, it would be interesting to test macroporous perovskites such as $La_2NiB'O_6$ in DRM, as, to the best of our knowledge, this has not yet been carried out.

Author Contributions: Conceptualization, A.G.G., N.D.C. and M.A.G.; methodology, A.G.G.; investigation, A.G.G.; formal analysis, A.G.G. and N.D.C.; funding acquisition, M.A.G.; writing—review and editing, A.G.G., N.D.C. and M.A.G. All authors have read and agreed to the published version of the manuscript.

Funding: The authors gratefully acknowledge that this research has been co-financed by the European Union and Greek national funds under the call "Greece—China Call for Proposals for Joint RT&D Projects" (Project Code: T7DKI-00388).

Data Availability Statement: The data presented in this study are available upon request from the corresponding author.

Conflicts of Interest: The authors declare no conflict of interest.

References

1. Ahmand, T.; Zhang, D. A critical review of comparative global historical energy consumption and future demand: The story told so far. *Energy Rep.* **2020**, *6*, 1973–1991. [CrossRef]
2. Veziroğlu, T.N.; Şahin, S. 21st Century's energy: Hydrogen energy system. *Energy Convers. Manag.* **2008**, *49*, 1820–1831. [CrossRef]
3. Latsiou, A.I.; Charisiou, N.D.; Frontistis, Z.; Bansode, A.; Goula, M.A. CO_2 hydrogenation for the production of higher alcohols: Recent trends, challenges and opportunities. *Catal. Today* **2023**, *420*, 114179. [CrossRef]
4. Bergero, C.; Rich, M.J.; Saikawa, E. All roads lead to Paris: The eight pathways to renewable energy target adoption. *Energy Res. Soc. Sci.* **2021**, *80*, 102215. [CrossRef]
5. Zandalinas, S.I.; Fritschi, F.B.; Mittler, R. Global Warming, Climate Change, and Environmental Pollution: Recipe for a Multifactorial Stress Combination Disaster. *Trends Plant Sci.* **2021**, *6*, 588–599. [CrossRef] [PubMed]
6. Yaduvanshi, A.; Nkemelang, T.; Bendapundi, R.; New, M. Temperature and rainfall extremes change under current and future global warming levels across Indian climate zones. *Weather. Clim. Extrem.* **2021**, *31*, 100291. [CrossRef]
7. Swain, D.L.; Singh, D.; Touma, D.; Diffenbaugh, N.S. Attributing Extreme Events to Climate Change: A New Frontier in a Warming World. *One Earth* **2020**, *2*, 522–527. [CrossRef]
8. Shi, X.; Chen, J.; Gu, L.; Xu, C.Y.; Chen, H.; Zhang, L. Impacts and socioeconomic exposures of global extreme precipitation events in 1.5 and 2.0 °C warmer climates. *Sci. Total Environ.* **2021**, *766*, 142665. [CrossRef] [PubMed]
9. Ahmad, N.; Alharthi, F.; Alam, M.; Wahab, R.; Manoharadas, S.; Alrayes, B. Syngas production via CO_2 reforming of methane over $SrNiO_3$ and $CeNiO_3$ perovskites. *Energies* **2021**, *14*, 2928. [CrossRef]
10. Rabelo-Neto, R.C.; Sales, H.B.E.; Inocêncio, C.V.M.; Varga, E.; Oszko, A.; Erdohelyi, A.; Noronha, F.B.; Mattos, L.V. CO_2 reforming of methane over supported $LaNiO_3$ perovskite-type oxides. *Appl. Catal. B Environ.* **2018**, *221*, 349–361. [CrossRef]
11. Goula, M.A.; Charisiou, N.D.; Papageridis, K.N.; Delimitis, A.; Pachatouridou, E.; Iliopoulou, E.F. Nickel on alumina catalysts for the production of hydrogen rich mixtures via the biogas dry reforming reaction: Influence of the synthesis method. *Int. J. Hydrogen Energy* **2015**, *40*, 9183–9200. [CrossRef]
12. Goula, M.A.; Charisiou, N.D.; Siakavelas, G.; Tzounis, L.; Tsiaoussis, I.; Panagiotopoulou, P.; Goula, G.; Yentekakis, I.V. Syngas production via the biogas dry reforming reaction over Ni supported on zirconia modified with CeO_2 or La_2O_3 catalysts. *Int. J. Hydrogen Energy* **2017**, *42*, 13724–13740. [CrossRef]
13. Field, R.A.; Derwent, R.G. Global warming consequences of replacing natural gas with hydrogen in the domestic energy sectors of future low-carbon economies in the United Kingdom and the United States of America. *Int. J. Hydrogen Energy* **2021**, *46*, 30190–30203. [CrossRef]
14. Acar, C.; Dincer, I. The potential role of hydrogen as a sustainable transportation fuel to combat global warming. *Int. J. Hydrogen Energy* **2020**, *45*, 3396–3406. [CrossRef]
15. Latsiou, A.I.; Bereketidou, O.A.; Charisiou, N.D.; Georgiadis, A.G.; Avraam, D.G.; Goula, M.A. Synthesis and mathematical modelling of the preparation process of nickel-alumina catalysts with egg/shell structures for hydrogen syngas production via reforming of clean model biogas. *Catalysts* **2022**, *12*, 274. [CrossRef]
16. Charisiou, N.D.; Siakavelas, G.; Papageridis, K.; Baklavaridis, A.; Tzounis, L.; Goula, G.; Yentekakis, I.V.; Goula, M.A. The effect of WO_3 modification of ZrO_2 support on the Ni-catalyzed dry reforming of biogas reaction for syngas production. *Front. Environ. Sci.* **2017**, *5*, 66. [CrossRef]
17. Charisiou, N.D.; Baklavaridis, A.; Papadakis, V.G.; Goula, M.A. Synthesis gas production via the biogas reforming reaction over $Ni/MgO-Al_2O_3$ and $Ni/CaO-Al_2O_3$ catalysts. *Waste Biomass Valorization* **2016**, *7*, 725–736. [CrossRef]
18. Taipadu, M.I.; Viswanathan, K.; Wu, W.; Hattu, N.; Atabani, A.E. A critical review of the hydrogen production from biomass-based feedstocks: Challenge, solution, and future prospect. *Process. Saf. Environ.* **2022**, *164*, 384–407. [CrossRef]
19. Polychronopoulou, K.; Dabbawala, A.; Sajjad, M.; Singh, N.; Anjum, D.H.; Baker, M.A.; Charisiou, N.D.; Goula, M.A. Exploring the potential of Ce-La-Cu-O oxide towards hydrogen production via steam reforming of glycerol: An experimental and DFT study. *Appl. Surf. Sci.* **2022**, *586*, 152798. [CrossRef]
20. Charisiou, N.D.; Siakavelas, G.; Dou, B.; Sebastian, V.; Baker, M.A.; Hinder, S.J.; Polychronopoulou, K.; Goula, M.A. Nickel Supported on $AlCeO_3$ as a Highly Selective and Stable Catalyst for Hydrogen Production via the Glycerol Steam Reforming Reaction. *Catalysts* **2019**, *9*, 411. [CrossRef]
21. Shahbaz, M.; Al-Ansari, T.; Aslam, M.; Khan, Z.; Inayat, A.; Athar, M.; Naqvi, S.R.; Ahmed, M.A.; McKay, G. A state of the art review on biomass processing and conversion technologies to produce hydrogen and its recovery via membrane separation. *Int. J. Hydrogen Energy* **2020**, *45*, 15166–15195. [CrossRef]
22. Lino, A.V.P.; Assaf, E.M.; Assaf, J.M. Adjusting Process Variables in Methane Tri-reforming to Achieve Suitable Syngas Quality and Low Coke Deposition. *Energy Fuel.* **2020**, *12*, 16522–16531. [CrossRef]
23. Yentekakis, I.V.; Panagiotopoulou, P.; Artemakis, G. A review of recent efforts to promote dry reforming of methane (DRM) to syngas production via bimetallic catalyst formulations. *Appl. Catal. B Environ.* **2021**, *296*, 120210. [CrossRef]
24. Roy, P.S.; Song, J.; Kim, K.; Park, C.S.; Raju, A.S.K. CO_2 conversion to syngas through the steam-biogas reforming process. *J. CO_2 Util.* **2018**, *25*, 275–282. [CrossRef]

25. Dehimi, L.; Gaillard, M.; Virginie, M.; Erto, A.; Benguerba, Y. Investigation of dry reforming of methane over Mo-based catalysts. *Int. J. Hydrogen Energy* **2020**, *45*, 24657–24669. [CrossRef]
26. Roy, P.S.; Park, C.S.; Raju, A.S.K.; Kim, K. Steam-biogas reforming over a metal-foam-coated (Pd-Rh)/($CeZrO_2$-Al_2O_3) catalyst compared with pellet type alumina-supported Ru and Ni catalysts. *J. CO_2 Util.* **2021**, *12*, 12–20. [CrossRef]
27. Zagaynov, I.V.; Loktev, A.S.; Mukhin, I.E.; Konovalov, A.A.; Dedov, A.G.; Moiseev, I.I. Trimetallic NiCoM catalysts (M = Mn, Fe, Cu) for methane conversion into synthesis gas. *Mendeleev Commun.* **2019**, *29*, 22–24. [CrossRef]
28. Charisiou, N.D.; Siakavelas, G.; Tzounis, L.; Sebastian, V.; Monzon, A.; Baker, M.A.; Hinder, S.J.; Polychronopoulou, K.; Yentekakis, I.V.; Goula, M.A. An in depth investigation of deactivation through carbon formation during the biogas dry reforming reaction for Ni supported on modified with CeO_2 and La_2O_3 zirconia catalysts. *Int. J. Hydrogen Energy* **2018**, *43*, 18955–18976. [CrossRef]
29. Bian, Z.; Das, S.; Wai, M.H.; Hongmanorom, P.; Kawi, S. A Review on Bimetallic Nickel-Based Catalysts for CO_2 Reforming of Methane. *ChemPhysChem* **2017**, *18*, 3117–3134. [CrossRef]
30. Das, S.; Ashok, J.; Bian, Z.; Dewangan, N.; Wai, M.H.; Du, Y.; Borgna, A.; Hidajat, K.; Kawi, S. Silica–Ceria sandwiched Ni core–shell catalyst for low temperature dry reforming of biogas: Coke resistance and mechanistic insights. *Appl. Catal. B Environ.* **2018**, *230*, 220–236. [CrossRef]
31. Murakami, M.; Ohishi, Y.; Hirao, N.; Hirose, K. A perovskitic lower mantle inferred from high-pressure, high-temperature sound velocity data. *Nature* **2012**, *485*, 90–94. [CrossRef] [PubMed]
32. Sim, Y.; Kwon, D.; An, S.; Ha, J.M.; Oh, T.S.; Jung, J.C. Catalytic behavior of ABO_3 perovskites in the oxidative coupling of methane. *Mol. Catal.* **2020**, *489*, 110925. [CrossRef]
33. Royer, S.; Duprez, D.; Can, F.; Courtois, X.; Batiot-Dupeyrat, C.; Laassiri, S.; Alamdari, H. Perovskiets as Substitutes of Noble Metals for Heterogeneous Catalysis: Dream or Reality. *Chem. Rev.* **2014**, *20*, 10292–10368. [CrossRef] [PubMed]
34. Yadav, P.; Yadav, S.; Atri, S.; Tomar, R. A Brief Review on Key Role of Perovskite Oxides as Catalyst. *ChemistryEurope* **2021**, *6*, 12947–12959. [CrossRef]
35. Bian, Z.; Wang, Z.; Jiang, B.; Hongmanorom, P.; Zhong, W.; Kawi, S. A review on perovskite catalysts for reforming of methane to hydrogen production. *Renew. Sustain. Energy Rev.* **2020**, *134*, 110291. [CrossRef]
36. Bhattar, S.; Abedin, M.A.; Kanitkar, S.; Spivey, J.J. A review on dry reforming of methane over perovskite derived catalysts. *Catal. Today* **2021**, *365*, 2–23. [CrossRef]
37. Hou, Z.; Chen, P.; Fang, H.; Zheng, X.; Yashima, T. Production of synthesis gas via methane reforming with CO_2 on noble metals and small amount of noble-(Rh-) promoted Ni catalysts. *Int. J. Hydrogen Energy* **2006**, *31*, 555–561. [CrossRef]
38. Charisiou, N.D.; Iordanidis, A.; Polychronopoulou, K.; Yentekakis, I.V.; Goula, M.A. Studying the stability of Ni supported on modified with CeO_2 alumina catalysts for the biogas dry reforming reaction. *Mater. Today Proc.* **2018**, *5*, 27607–27616. [CrossRef]
39. Charisiou, N.D.; Douvartzides, S.L.; Siakavelas, G.I.; Tzounis, L.; Sebastian, V.; Stolojan, V.; Hinder, S.J.; Baker, M.A.; Polychronopoulou, K.; Goula, M.A. The relationship between reaction temperature and carbon deposition on nickel catalysts based on Al_2O_3, ZrO_2 or SiO_2 supports during the biogas dry reforming reaction. *Catalysts* **2019**, *9*, 676. [CrossRef]
40. Charisiou, N.D.; Tzounis, L.; Sebastian, V.; Baker, M.A.; Hinder, S.J.; Polychronopoulou, K.; Goula, M.A. Investigating the correlation between deactivation and the carbon deposited on the surface of Ni/Al_2O_3 and Ni/La_2O_3-Al_2O_3 catalysts during the biogas reforming reaction. *Appl. Surf. Sci.* **2019**, *474*, 42–56. [CrossRef]
41. Ruocco, C.; De Caprariis, B.; Palma, V.; Petrullo, A.; Ricca, A.; Scarsella, M.; De Filippis, P. Methane dry reforming on Ru perovskites, $AZrRuO_3$: Influence of preparation method and substitution of A cation with alkaline earth metals. *J. CO_2 Util.* **2019**, *30*, 222–231. [CrossRef]
42. Silva, C.K.S.; Baston, E.P.; Melgar, L.Z.; Bellido, J.D.A. Ni/Al_2O_3-La_2O_3 catalysts synthesized by a one-step polymerization method applied to the dry reforming of methane: Effect of precursor structures of nickel, perovskite and spinel. *React. Kinet. Mech. Catal.* **2019**, *128*, 251–269. [CrossRef]
43. Oar-Arteta, L.; Remiro, A.; Vicente, J.; Aguayo, A.T.; Bilbao, J.; Gayubo, A.G. Stability of $CuZnOAl_2O_3$/HZSM-5 and CuFe $2O_4$/HZSM-5 catalysts in dimethyl ether steam reforming operating in reaction-regeneration cycles. *Fuel Process. Technol.* **2014**, *126*, 145–154. [CrossRef]
44. Charisiou, N.D.; Siakavelas, G.; Papageridis, K.N.; Baklavaridis, A.; Tzounis, L.; Avraam, D.G.; Goula, M.A. Syngas production via the biogas dry reforming reaction over nickel supported on modified with CeO_2 and/or La_2O_3 alumina catalysts. *J. Nat. Gas. Sci. Eng.* **2016**, *31*, 164–183. [CrossRef]
45. Bereketidou, O.A.; Goula, M.A. Biogas reforming for syngas production over nickel supported on ceria-alumina catalysts. *Catal. Today* **2012**, *195*, 93–100. [CrossRef]
46. Wu, C.; Liu, R. Carbon deposition behavior in steam reforming of bio-oil model compound for hydrogen production. *Int. J. Hydrogen Energy* **2010**, *35*, 7386–7398. [CrossRef]
47. Sutthiumporn, K.; Kawi, S. Promotional effect of alkaline earth over Ni-La_2O_3 catalyst for CO_2 reforming of CH_4: Role of surface oxygen species on H_2 production and carbon suppression. *Int. J. Hydrogen Energy* **2011**, *36*, 14435–14446. [CrossRef]
48. Li, L.; Chen, J.; Zhang, Q.; Yang, Z.; Sun, Y.; Zou, G. Methane dry reforming over activated carbon supported Ni-catalysts prepared by solid phase synthesis. *J. Clean. Prod.* **2020**, *274*, 122256. [CrossRef]
49. Xu, L.; Song, H.; Chou, L. One-pot synthesis of ordered mesoporous NiO-CaO-Al_2O_3 composite oxides for catalyzing CO_2 reforming of CH_4. *ACS Catal.* **2012**, *2*, 1331–1342. [CrossRef]

50. Wang, Z.; Cao, X.M.; Zhu, J.; Hu, P. Activity and coke formation of nickel and nickel carbide in dry reforming: A deactivation scheme from density functional theory. *J. Catal.* **2014**, *311*, 469–480. [CrossRef]
51. Hu, Y.H.; Ruckenstein, E. Catalytic Conversion of Methane to Synthesis Gas by Partial Oxidation and CO_2 Reforming. *Adv. Catal.* **2004**, *48*, 297–345.
52. Bian, Z.; Kawi, S. Preparation, characterization and catalytic application of phyllosilicate: A review. *Catal. Today* **2020**, *339*, 3–23. [CrossRef]
53. Zhang, C.; Yue, H.; Huang, Z.; Li, S.; Wu, G.; Ma, X.; Gong, J. Hydrogen production via steam reforming of ethanol on phyllosilicate-derived Ni/SiO_2: Enhanced metal-support interaction and catalytic stability. *ACS Sustain. Chem. Eng.* **2013**, *1*, 161–173. [CrossRef]
54. Ashok, J.; Bian, Z.; Wang, Z.; Kawi, S. Ni-phyllosilicate structure derived Ni-SiO_2-MgO catalysts for bi-reforming applications: Acidity, basicity and thermal stability. *Catal. Sci. Technol.* **2018**, *8*, 1730–1742. [CrossRef]
55. Aramouni, N.A.K.; Touma, J.G.; Tarboush, B.A.; Zeaiter, J.; Ahmad, M.N. Catalyst design for dry reforming of methane: Analysis review. *Renew. Sustain. Energy Rev.* **2018**, *82*, 2570–2585. [CrossRef]
56. Jang, W.J.; Shim, J.O.; Kim, H.M.; Yoo, S.Y.; Roh, H.S. A review on dry reforming of methane in aspect of catalytic properties. *Catal. Today* **2019**, *324*, 15–26. [CrossRef]
57. Li, Z.; Li, M.; Ashok, J.; Kawi, S. NiCo@NiCo phyllosilicate@CeO_2 hollow core shell catalysts for steam reforming of toluene as biomass tar model compound. *Energy Convers. Manag.* **2019**, *180*, 822–830. [CrossRef]
58. Ganesh, I. A review on magnesium aluminate ($MgAl_2O_4$) spinel: Synthesis, processing and applications. *Int. Mater. Rev.* **2013**, *58*, 63–112. [CrossRef]
59. Grzybek, G.; Wójcik, S.; Ciura, K.; Gryboś, J.; Indyka, P.; Oszajca, M.; Stelmachowski, P.; Witkowski, S.; Inger, M.; Wilk, M.; et al. Influence of preparation method on dispersion of cobalt spinel over alumina extrudates and the catalyst deN_2O activity. *Appl. Catal. B Environ.* **2017**, *210*, 34–44. [CrossRef]
60. Cho, E.; Lee, Y.H.; Kim, H.; Jang, E.J.; Kwak, J.H.; Lee, K.; Ko, C.H.; Yoon, W.L. Ni catalysts for dry methane reforming prepared by A-site exsolution on mesoporous defect spinel magnesium aluminate. *Appl. Catal. A Gen.* **2020**, *602*, 117694. [CrossRef]
61. Bonmassar, N.; Bekheet, M.F.; Schlicker, L.; Gili, A.; Gurlo, A.; Doran, A.; Gao, Y.; Heggen, M.; Bernardi, J.; Klötzer, B.; et al. In Situ-Determined Catalytically Active State of $LaNiO_3$ in Methane Dry Reforming. *ACS Catal.* **2020**, *10*, 1102–1112. [CrossRef]
62. Komarala, E.P.; Komissarov, I.; Rosen, B.A. Effect of Fe and Mn substitution in $LaNiO_3$ on exsolution, activity, and stability for methane dry reforming. *Catalysts* **2020**, *10*, 27. [CrossRef]
63. Sellam, D.; Ikkour, K.; Dekkar, S.; Messaoudi, H.; Belaid, T.; Roger, A.C. CO_2 reforming of methane over $LaNiO_3$ perovskite supported catalysts: Influence of silica support. *Bull. Chem. React. Eng. Catal.* **2019**, *14*, 568–578. [CrossRef]
64. Bashan, V.; Ust, Y. Perovskite catalysts for methane combustion: Applications, design, effects for reactivity and partial oxidation. *Int. J. Energy Res.* **2019**, *43*, 7755–7789. [CrossRef]
65. Latsiou, A.; Lykos, C.; Bairamis, F.; Konstantinou, I. Synthesis and characterization of $LaCo_xNi_{1-x}O_3$ perovskites as heterogeneous catalysts for phenolics degradation by persulfate activation. *J. Chem. Technol. Biotechnol.* **2022**, *97*, 3467–3480. [CrossRef]
66. Tsiotsias, A.; Charisiou, N.D.; AlKhoori, A.; Gaber, S.; Sebastian, V.; Hinder, S.J.; Baker, M.A.; Polychronopoulou, K.; Goula, M.A. Towards maximizing conversion of ethane and carbon dioxide into synthesis gas using highly stable Ni/perovskite catalysts. *J. CO_2 Util.* **2022**, *61*, 102046. [CrossRef]
67. Oh, J.H.; Kwon, B.W.; Cho, J.; Lee, C.H.; Kim, M.K.; Choi, S.H.; Yoon, S.P.; Han, J.; Nam, S.W.; Kim, J.Y.; et al. Importance of Exsolution in Transition-Metal (Co, Rh, and Ir)-Doped $LaCrO_3$ Perovskite Catalysts for Boosting Dry Reforming of CH_4 Using CO_2 for Hydrogen Production. *Ind. Eng. Chem. Res.* **2019**, *58*, 6385–6393. [CrossRef]
68. Georgiadis, A.G.; Siakavelas, G.; Tsiotsias, A.; Charisiou, N.D.; Wang, W.; Sebastian, V.; Hinder, J.; Baker, M.A.; Mascotto, S.; Goula, M.A. Biogas Dry Reforming Over Ni/LnO_x-type catalysts (Ln = La, Ce, Sm or Pr). *Int. J. Hydrogen Energy* **2023**, *48*, 19953–19971. [CrossRef]
69. Rudolph, B.; Tsiotsias, A.; Ehrhardt, B.; Gross, S.; Dolcet, P.; Haas, S.; Charisiou, N.D.; Goula, M.A.; Mascotto, S. Nanoparticle exsolution from nanoporous perovskites for highly active and stable biogas dry reforming catalysts. *Adv. Sci.* **2023**, *10*, 2205890. [CrossRef]
70. Zhu, H.; Zhang, P.; Dai, S. Recent Advances of Lanthanum-Based Perovskite Oxides for Catalysis. *ACS Catal.* **2015**, *5*, 6370–6385. [CrossRef]
71. Zhu, J.; Li, H.; Zhong, L.; Xiao, P.; Xu, X.; Yang, X.; Zhao, Z.; Li, J. Perovskite oxides: Preparation, characterizations, and applications in heterogeneous catalysis. *ACS Catal.* **2014**, *4*, 2917–2940. [CrossRef]
72. Liu, C.; Chen, D.; Ashok, J.; Hongmanorom, P.; Wang, W.; Li, T.; Wang, Z.; Kawi, S. Chemical looping steam reforming of bio-oil for hydrogen-rich syngas production: Effect of doping on $LaNi_{0.8}Fe_{0.2}O_3$ perovskite. *Int. J. Hydrogen Energy* **2020**, *45*, 21123–21137. [CrossRef]
73. Goula, M.A.; Charisiou, N.D.; Pandis, P.K.; Stathopoulos, V.N. Ni/apatite-type lanthanum silicate supported catalyst for the glycerol steam reforming reaction. *RSC Adv.* **2016**, *6*, 78954–78958. [CrossRef]
74. Valderrama, G.; Kiennemann, A.; de Navarro, C.U.; Goldwasser, M.R. $LaNi_{1-x}Mn_xO_3$ perovskite-type oxides as catalysts precursors for dry reforming of methane. *Appl. Catal. A Gen.* **2018**, *565*, 26–33. [CrossRef]

75. Tsiotsias, A.; Ehrhardt, B.; Rudolph, B.; Nodari, L.; Kim, S.; Jung, W.; Charisiou, N.D.; Goula, M.A.; Mascotto, S. Modulating bimetallic Fe-Ni exsolution to tune the CO_2-assisted ethane dehydrogenation and reforming pathways. *ACS Nano* **2022**, *16*, 8904–8916. [CrossRef]
76. Ismaila, A.; Chen, X.; Gao, X.; Fan, X. Thermodynamic analysis of steam reforming of glycerol for hydrogen production at atmospheric pressure. *Front. Chem. Sci. Eng.* **2021**, *15*, 60–71. [CrossRef]
77. Zhang, Z.; Verykios, X.E.; MacDonald, S.M.; Affrossman, S. Comparative study of carbon dioxide reforming of methane to synthesis gas over Ni/La_2O_3 and conventional nickel-based catalysts. *J. Phys. Chem.* **1996**, *100*, 744–754. [CrossRef]
78. Provendier, H.; Petif, C.; Estournes, C.; Kiennemann, A. Dry reforming of methane. Interest of La-Ni-Fe solid solutions compared to $LaNiO_3$ and $LaFeO_3$. *Stud. Surf. Sci. Catal.* **1998**, *119*, 741–746.
79. Batiot-Dupeyrat, C.; Gallego, G.A.S.; Mondragon, F.; Barrault, J.; Tatibouët, J.M. CO_2 reforming of methane over $LaNiO_3$ as precursor material. *Catal. Today* **2005**, *107–108*, 474–480. [CrossRef]
80. Cao, D.; Luo, C.; Cai, G.; Luo, T.; Wu, F.; Li, X.; Zheng, Y.; Zhang, L. Development and Regeneration Performance of $LaNiO_3$ Perovskite Oxides for Dry Reforming of Methane. *J. Therm. Sci.* **2023**, *32*, 1935–1944. [CrossRef]
81. Batiot-Dupeyrat, C.; Valderrama, G.; Meneses, A.; Martinez, F.; Barrault, J.; Tatibouët, J.M. Pulse study of CO_2 reforming of methane over $LaNiO_3$. *Appl. Catal. A Gen.* **2003**, *248*, 143–151. [CrossRef]
82. Gallego, G.S.; Batiot-Dupeyrat, C.; Barrault, J.; Mondragón, F. Dual active-site mechanism for dry methane reforming over Ni/La_2O_3 produced from $LaNiO_3$ perovskite. *Ind. Eng. Chem. Res.* **2008**, *47*, 9272–9278. [CrossRef]
83. Gallego, G.S.; Mondragón, F.; Barrault, J.; Tatibouët, J.M.; Batiot-Dupeyrat, C. CO_2 reforming of CH_4 over La-Ni based perovskite precursors. *Appl. Catal. A Gen.* **2006**, *311*, 164–171. [CrossRef]
84. Pereñiguez, R.; Gonzalez-delaCruz, V.M.; Caballero, A.; Holgado, J.P. $LaNiO_3$ as a precursor of Ni/La_2O_3 for CO_2 reforming of CH_4: Effect of the presence of an amorphous NiO phase. *Appl. Catal. B Environ.* **2012**, *123–124*, 324–332. [CrossRef]
85. Chawla, S.K.; George, M.; Patel, F.; Patel, S. Production of synthesis gas by carbon dioxide reforming of methane over nickel based and perovskite catalysts. *Procedia Eng.* **2013**, *51*, 461–466. [CrossRef]
86. Maneerung, T.; Hidajat, K.; Kawi, S. $LaNiO_3$ perovskite catalyst precursor for rapid decomposition of methane: Influence of temperature and presence of H_2 in feed stream. *Catal. Today* **2011**, *171*, 24–35. [CrossRef]
87. Kuras, M.; Zimmermann, Y.; Petit, C. Reactivity of perovskite-type precursor in MWCNTs synthesis. *Catal. Today* **2008**, *138*, 55–61. [CrossRef]
88. Valderrama, G.; Goldwasser, M.R.; De Navarro, C.U.; Tatibouët, J.M.; Barrault, J.; Batiot-Dupeyrat, C.; Martínez, F. Dry reforming of methane over Ni perovskite type oxides. *Catal. Today* **2005**, *107–108*, 785–791. [CrossRef]
89. Papargyriou, D.; Miller, D.N.; Irvine, J.T.S. Exsolution of Fe-Ni alloy nanoparticles from (La,Sr)(Cr,Fe,Ni)O_3 perovskites as potential oxygen transport membrane catalysts for methane reforming. *J. Mater. Chem. A* **2019**, *7*, 15812–15822. [CrossRef]
90. Yang, E.H.; Moon, D.J. Synthesis of $LaNiO_3$ perovskite using an EDTA-cellulose method and comparison with the conventional Pechini method: Application to steam CO_2 reforming of methane. *RSC Adv.* **2016**, *6*, 112885–112898. [CrossRef]
91. Singh, S.; Zubenko, D.; Rosen, B.A. Influence of $LaNiO_3$ Shape on Its Solid-Phase Crystallization into Coke-Free Reforming Catalysts. *ACS Catal.* **2016**, *6*, 4199–4205. [CrossRef]
92. Yang, E.H.; Moon, D.J. CO_2 Reforming of Methane over Ni^0/La_2O_3 Catalyst Without Reduction Step: Effect of Calcination Atmosphere. *Top. Catal.* **2017**, *60*, 697–705. [CrossRef]
93. Oliveira, Â.A.S.; Medeiros, R.L.B.A.; Figueredo, G.P.; Macedo, H.P.; Braga, R.M.; Maziviero, F.V.; Melo, M.A.F.; Melo, D.M.A.; Vieira, M.M. One-step synthesis of $LaNiO_3$ with chitosan for dry reforming of methane. *Int. J. Hydrogen Energy* **2018**, *43*, 9696–9704. [CrossRef]
94. Chai, Y.; Fu, Y.; Feng, H.; Kong, W.; Yuan, C.; Pan, B.; Zhang, J.; Sun, Y. A Nickel-Based perovskite catalyst with a bimodal size distribution of Nickel particles for dry reforming of methane. *ChemCatChem* **2018**, *10*, 2078–2086. [CrossRef]
95. Pereñíguez, R.; González-DelaCruz, V.M.; Holgado, J.P.; Caballero, A. Synthesis and characterization of a $LaNiO_3$ perovskite as precursor for methane reforming reactions catalysts. *Appl. Catal. B Environ.* **2010**, *93*, 346–353. [CrossRef]
96. Dama, S.; Ghodke, S.R.; Bobade, R.; Gurav, H.R.; Chilukuri, S. Active and durable alkaline earth metal substituted perovskite catalysts for dry reforming of methane. *Appl. Catal. B Environ.* **2018**, *224*, 146–158. [CrossRef]
97. Moradi, G.R.; Rahmanzadeh, M. The influence of partial substitution of alkaline earth with la in the $LaNiO_3$ perovskite catalyst. *Catal. Commun.* **2012**, *26*, 169–172. [CrossRef]
98. De Lima, S.M.; Peña, M.A.; Fierro, J.L.G.; Assaf, J.M. $La_{1-x}Ca_xNiO_3$ perovskite oxides: Characterization and catalytic reactivity in dry reforming of methane. *Catal. Letters* **2008**, *124*, 195–203. [CrossRef]
99. Khalesi, A.; Arandiyan, H.R.; Parvari, M. Effects of lanthanum substitution by strontium and calcium in La-Ni-Al perovskite oxides in dry reforming of methane. *Chin. J. Catal.* **2008**, *29*, 960–968. [CrossRef]
100. Gallego, G.S.; Marín, J.G.; Batiot-Dupeyrat, C.; Barrault, J.; Mondragón, F. Influence of Pr and Ce in dry methane reforming catalysts produced from $La_{1-x}A_xNiO_{3-\delta}$ perovskites. *Appl. Catal. A Gen.* **2009**, *369*, 97–103. [CrossRef]
101. Su, Y.J.; Pan, K.L.; Chang, M.B. Modifying perovskite-type oxide catalyst $LaNiO_3$ with Ce for carbon dioxide reforming of methane. *Int. J. Hydrogen Energy* **2014**, *39*, 4917–4925. [CrossRef]
102. Lima, S.M.; Assaf, J.M.; Peña, M.A.; Fierro, J.L.G. Structural features of $La_{1-x}Ce_xNiO_3$ mixed oxides and performance for the dry reforming of methane. *Appl. Catal. A Gen.* **2006**, *311*, 94–104. [CrossRef]

103. Wang, M.; Zhao, T.; Dong, X.; Li, M.; Wang, H. Effects of Ce substitution at the A-site of $LaNi_{0.5}Fe_{0.5}O_3$ perovskite on the enhanced catalytic activity for dry reforming of methane. *Appl. Catal. B Environ.* **2018**, *224*, 214–221. [CrossRef]
104. Siakavelas, G.I.; Charisiou, N.D.; AlKhoori, A.; Sebastian, V.; Hinder, S.J.; Baker, M.A.; Yentekakis, I.V.; Polychronopoulou, K.; Goula, M.A. Cerium Oxide Catalysts for Oxidative Coupling of Methane: Effect of Lithium, Samarium and Lanthanum Dopants. *J. Environ. Chem. Eng.* **2022**, *10*, 107259. [CrossRef]
105. Siakavelas, G.I.; Charisiou, N.D.; AlKhoori, A.; AlKhoori, S.; Sebastian, V.; Hinder, S.J.; Baker, M.A.; Yentekakis, I.V.; Polychronopoulou, K.; Goula, M.A. Highly selective and stable Ni/La-M (M=Sm, Pr, and Mg)-CeO_2 catalysts for CO_2 methanation. *J. CO_2 Util.* **2021**, *51*, 101618. [CrossRef]
106. Yang, E.H.; Noh, Y.S.; Hong, G.H.; Moon, D.J. Combined steam and CO_2 reforming of methane over $La_{1-x}Sr_xNiO_3$ perovskite oxides. *Catal. Today* **2018**, *299*, 242–250. [CrossRef]
107. Rynkowski, J.; Samulkiewicz, P.; Ladavos, A.K.; Pomonis, P.J. Catalytic performance of reduced $La_{2-x}Sr_xNiO_4$ perovskite-like oxides for CO_2 reforming of CH_4. *Appl. Catal. A Gen.* **2004**, *263*, 1–9. [CrossRef]
108. Du, X.; Zhang, D.; Shi, L.; Gao, R.; Zhang, J. Morphology dependence of catalytic properties of Ni/CeO_2 nanostructures for carbon dioxide reforming of methane. *J. Phys. Chem. C* **2012**, *116*, 10009–10016. [CrossRef]
109. Moradi, G.R.; Rahmanzadeh, M.; Khosravian, F. The effects of partial substitution of Ni by Zn in $LaNiO_3$ perovskite catalyst for methane dry reforming. *J. CO_2 Util.* **2014**, *6*, 7–11. [CrossRef]
110. De Araujo, G.C.; de Lima, S.M.; Assaf, J.M.; Peña, M.A.; Fierro, J.L.G.; do Carmo Rangel, M. Catalytic evaluation of perovskite-type oxide $LaNi_{1-x}Ru_xO_3$ in methane dry reforming. *Catal. Today* **2008**, *133–135*, 129–135. [CrossRef]
111. Song, X.; Dong, X.; Yin, S.; Wang, M.; Li, M.; Wang, H. Effects of Fe partial substitution of La_2NiO_4/$LaNiO_3$ catalyst precursors prepared by wet impregnation method for the dry reforming of methane. *Appl. Catal. A Gen.* **2016**, *526*, 132–138. [CrossRef]
112. Moradi, G.R.; Khosravian, F.; Rahmanzadeh, M. Effects of partial substitution of Ni by Cu in $LaNiO_3$ perovskite catalyst for dry methane reforming. *Chin. J. Catal.* **2012**, *33*, 797–801. [CrossRef]
113. Wang, M.; Zhao, T.; Li, M.; Wang, H. Perovskite $La_2(NiCu)O_4$ catalyst precursors for dry reforming of methane: Effects of Cu-substitution on carbon resistance. *RSC Adv.* **2017**, *7*, 41847–41854. [CrossRef]
114. Shahnazi, A.; Firoozi, S. Improving the catalytic performance of $LaNiO_3$ perovskite by manganese substitution via ultrasonic spray pyrolysis for dry reforming of methane. *J. CO_2 Util.* **2021**, *45*, 101455. [CrossRef]
115. Oemar, U.; Kathiraser, Y.; Ang, M.L.; Hidajat, K.; Kawi, S. Catalytic biomass gasification to syngas over highly dispersed lanthanum-doped nickel on SBA-15. *ChemCatChem* **2015**, *7*, 3376–3385. [CrossRef]
116. Oemar, U.; Kathiraser, Y.; Mo, L.; Ho, X.K.; Kawi, S. CO_2 reforming of methane over highly active La-promoted Ni supported on SBA-15 catalysts: Mechanism and kinetic modelling. *Catal. Sci. Technol.* **2016**, *6*, 1173–1186. [CrossRef]
117. De Lima, S.M.; Assaf, J.M. Ni-Fe catalysts based on perovskite-type oxides for dry reforming of methane to syngas. *Catal. Lett.* **2006**, *108*, 63–70. [CrossRef]
118. Dama, S.; Ghodke, S.; Bobade, R.; Gurav, H.; Chilukuri, S. Tuning the dimensionality of layered $Sr_{n+1}Ti_{n-x}Ni_xO_{3n+1}$ perovskite structures for improved activity in syngas generation. *J. Catal.* **2018**, *360*, 27–39. [CrossRef]
119. Rivas, M.E.; Fierro, J.L.G.; Goldwasser, M.R.; Pietri, E.; Pérez-Zurita, M.J.; Griboval-Constant, A.; Leclercq, G. Structural features and performance of $LaNi_{1-x}Rh_xO_3$ system for the dry reforming of methane. *Appl. Catal. A Gen.* **2008**, *344*, 10–19. [CrossRef]
120. Yasyerli, S.; Filizgok, S.; Arbag, H.; Yasyerli, N.; Dogu, G. Ru incorporated Ni-MCM-41 mesoporous catalysts for dry reforming of methane: Effects of Mg addition, feed composition and temperature. *Int. J. Hydrogen Energy* **2011**, *36*, 4863–4874. [CrossRef]
121. Zhou, H.; Zhang, T.; Sui, Z.; Zhu, Y.A.; Han, C.; Zhu, K.; Zhou, X. A single source method to generate Ru-Ni-MgO catalysts for methane dry reforming and the kinetic effect of Ru on carbon deposition and gasification. *Appl. Catal. B Environ.* **2018**, *233*, 143–159. [CrossRef]
122. Wang, L.; Chen, J.; Watanabe, H.; Xu, Y.; Tamura, M.; Nakagawa, Y.; Tomishige, K. Catalytic performance and characterization of Co-Fe bcc alloy nanoparticles prepared from hydrotalcite-like precursors in the steam gasification of biomass-derived tar. *Appl. Catal. B Environ.* **2014**, *160–161*, 701–715. [CrossRef]
123. Wang, L.; Li, D.; Koike, M.; Koso, S.; Nakagawa, Y.; Xu, Y.; Tomishige, K. Catalytic performance and characterization of Ni-Fe catalysts for the steam reforming of tar from biomass pyrolysis to synthesis gas. *Appl. Catal. A Gen.* **2011**, *392*, 248–255. [CrossRef]
124. Koike, M.; Li, D.; Nakagawa, Y.; Tomishige, K. A highly active and coke-resistant steam reforming catalyst comprising uniform nickel-iron alloy nanoparticles. *ChemSusChem* **2012**, *5*, 2312–2314. [CrossRef] [PubMed]
125. Jahangiri, A.; Aghabozorg, H.; Pahlavanzadeh, H. Effects of Fe substitutions by Ni in La-Ni-O perovskite-type oxides in reforming of methane with CO_2 and O_2. *Int. J. Hydrogen Energy* **2013**, *38*, 10407–10416. [CrossRef]
126. Tomishige, K.; Li, D.; Tamura, M.; Nakagawa, Y. Nickel-iron alloy catalysts for reforming of hydrocarbons: Preparation, structure, and catalytic properties. *Catal. Sci. Technol.* **2017**, *7*, 3952–3979. [CrossRef]
127. Theofanidis, S.A.; Galvita, V.V.; Poelman, H.; Marin, G.B. Enhanced carbon-resistant dry reforming Fe-Ni catalyst: Role of Fe. *ACS Catal.* **2015**, *5*, 3028–3039. [CrossRef]
128. Kim, S.M.; Abdala, P.M.; Margossian, T.; Hosseini, D.; Foppa, L.; Armutlulu, A.; Van Beek, W.; Comas-Vives, A.; Copéret, C.; Müller, C. Cooperativity and dynamics increase the performance of NiFe dry reforming catalysts. *J. Am. Chem. Soc.* **2017**, *139*, 1937–1949. [CrossRef]

129. Tsoukalou, A.; Imtiaz, Q.; Kim, S.M.; Abdala, P.M.; Yoon, S.; Müller, C.R. Dry-reforming of methane over bimetallic Ni–M/La_2O_3 (M = Co, Fe): The effect of the rate of $La_2O_2CO_3$ formation and phase stability on the catalytic activity and stability. *J. Catal.* **2016**, *343*, 208–214. [CrossRef]
130. Wang, Z.; Wang, C.; Chen, S.; Liu, Y. Co-Ni bimetal catalyst supported on perovskite-type oxide for steam reforming of ethanol to produce hydrogen. *Int. J. Hydrogen Energy* **2014**, *39*, 5644–5652. [CrossRef]
131. Urasaki, K.; Tokunaga, K.; Sekine, Y.; Matsukata, M.; Kikuchi, E. Production of hydrogen by steam reforming of ethanol over cobalt and nickel catalysts supported on perovskite-type oxides. *Catal. Commun.* **2008**, *9*, 600–604. [CrossRef]
132. Valderrama, G.; Kiennemann, A.; Goldwasser, M.R. Dry reforming of CH_4 over solid solutions of $LaNi_{1-x}Co_xO_3$. *Catal. Today* **2008**, *133–135*, 142–148. [CrossRef]
133. Mousavi, M.; Nakhaei Pour, A. Performance and structural features of $LaNi_{0.5}Co_{0.5}O_3$ perovskite oxides for the dry reforming of methane: Influence of the preparation method. *New J. Chem.* **2019**, *43*, 10763–10773. [CrossRef]
134. Touahra, F.; Rabahi, A.; Chebout, R.; Boudjemaa, A.; Lerari, D.; Sehailia, M.; Halliche, D.; Bachari, K. Enhanced catalytic behaviour of surface dispersed nickel on $LaCuO_3$ perovskite in the production of syngas: An expedient approach to carbon resistance during CO_2 reforming of methane. *Int. J. Hydrogen Energy* **2016**, *41*, 2477–2486. [CrossRef]
135. Wei, T.; Jia, L.; Zheng, H.; Chi, B.; Pu, J.; Li, J. $LaMnO_3$-based perovskite with in-situ exsolved Ni nanoparticles: A highly active, performance stable and coking resistant catalyst for CO_2 dry reforming of CH_4. *Appl. Catal. A Gen.* **2018**, *564*, 199–207. [CrossRef]
136. Kim, W.Y.; Jang, J.S.; Ra, E.C.; Kim, K.Y.; Kim, E.H.; Lee, J.S. Reduced perovskite $LaNiO_3$ catalysts modified with Co and Mn for low coke formation in dry reforming of methane. *Appl. Catal. A Gen.* **2019**, *575*, 198–203. [CrossRef]
137. Valderrama, G.; Kiennemann, A.; Goldwasser, M.R. La-Sr-Ni-Co-O based perovskite-type solid solutions as catalyst precursors in the CO_2 reforming of methane. *J. Power Sources* **2010**, *195*, 1765–1771. [CrossRef]
138. Sutthiumporn, K.; Maneerung, T.; Kathiraser, Y.; Kawi, S. CO_2 dry-reforming of methane over $La_{0.8}Sr_{0.2}Ni_{0.8}M_{0.2}O_3$ perovskite (M = Bi, Co, Cr, Cu, Fe): Roles of lattice oxygen on C-H activation and carbon suppression. *Int. J. Hydrogen Energy* **2012**, *37*, 11195–11207. [CrossRef]
139. Xiao, P.; Hong, J.; Wang, T.; Xu, X.; Yuan, Y.; Li, J.; Zhu, J. Oxidative degradation of organic dyes over supported perovskite Oxide $LaFeO_3$/SBA-15 under Ambient Conditions. *Catal. Lett.* **2013**, *143*, 887–894. [CrossRef]
140. Kathiraser, Y.; Thitsartarn, W.; Sutthiumporn, K.; Kawi, S. Inverse $NiAl_2O_4$ on $LaAlO_3$-Al_2O_3: Unique catalytic structure for stable CO_2 reforming of methane. *J. Phys. Chem. C* **2013**, *117*, 8120–8130. [CrossRef]
141. Yadav, P.K.; Das, T. Production of syngas from carbon dioxide reforming of methane by using $LaNi_xFe_{1-x}O_3$ perovskite type catalysts. *Int. J. Hydrogen Energy* **2019**, *44*, 1659–1670. [CrossRef]
142. Zhang, L.; Lian, J.; Li, L.; Peng, C.; Liu, W.; Xu, X.; Fang, X.; Wang, Z.; Wang, X.; Peng, H. $LaNiO_3$ nanocube embedded in mesoporous silica for dry reforming of methane with enhanced coking resistance. *Microporous Mesoporous Mater.* **2018**, *266*, 189–197. [CrossRef]
143. Wang, N.; Yu, X.; Wang, Y.; Chu, W.; Liu, M. A comparison study on methane dry reforming with carbon dioxide over $LaNiO_3$ perovskite catalysts supported on mesoporous SBA-15, MCM-41 and silica carrier. *Catal. Today* **2013**, *212*, 98–107. [CrossRef]
144. Rivas, I.; Alvarez, J.; Pietri, E.; Pérez-Zurita, M.J.; Goldwasser, M.R. Perovskite-type oxides in methane dry reforming: Effect of their incorporation into a mesoporous SBA-15 silica-host. *Catal. Today* **2010**, *149*, 388–393. [CrossRef]
145. Nair, M.M.; Kaliaguine, S.; Kleitz, F. Nanocast $LaNiO_3$ perovskites as precursors for the preparation of coke-resistant dry reforming catalysts. *ACS Catal.* **2014**, *4*, 3837–3846. [CrossRef]
146. Duan, Q.; Wang, J.; Ding, C.; Ding, H.; Guo, S.; Jia, Y.; Liu, P.; Zhang, K. Partial oxidation of methane over Ni based catalyst derived from order mesoporous $LaNiO_3$ perovskite prepared by modified nanocasting method. *Fuel* **2017**, *193*, 112–118. [CrossRef]
147. Ruan, Y.; Zhao, Y.; Lu, Y.; Guo, D.; Zhao, Y.; Wang, S.; Ma, X. Mesoporous $LaAl_{0.25}Ni_{0.75}O_3$ perovskite catalyst using SBA-15 as templating agent for methane dry reforming. *Microporous Mesoporous Mater.* **2020**, *303*, 110278. [CrossRef]
148. Messaoudi, H.; Thomas, S.; Djaidja, A.; Slyemi, S.; Barama, A. Study of La_xNiO_y and $La_xNiO_y/MgAl_2O_4$ catalysts in dry reforming of methane. *J. CO_2 Util.* **2018**, *24*, 40–49. [CrossRef]
149. Kärger, J.; Valiullin, R. Mass transfer in mesoporous materials: The benefit of microscopic diffusion measurement. *Chem. Soc. Rev.* **2013**, *42*, 4172–4197. [CrossRef]
150. Arandiyan, H.; Wang, Y.; Sun, H.; Rezaei, M.; Dai, H. Ordered meso- and macroporous perovskite oxide catalysts for emerging applications. *Chem. Commun.* **2018**, *54*, 6484–6502. [CrossRef]
151. Arandiyan, H.; Scott, J.; Wang, Y.; Dai, H.; Sun, H.; Amal, R. Meso-Molding Three-Dimensional Macroporous Perovskites: A New Approach to Generate High-Performance Nanohybrid Catalysts. *ACS Appl. Mater. Interfaces* **2016**, *8*, 2457–2463. [CrossRef]
152. Arandiyan, H.; Dai, H.; Deng, J.; Wang, Y.; Sun, H.; Xie, S.; Bai, B.; Liu, Y.; Ji, K.; Li, J. Three-dimensionally ordered macroporous $La_{0.6}Sr_{0.4}MnO_3$ supported Ag Nanoparticles for the combustion of methane. *J. Phys. Chem. C* **2014**, *118*, 14913–14928. [CrossRef]
153. Kathiraser, Y.; Oemar, U.; Saw, E.T.; Li, Z.; Kawi, S. Kinetic and mechanistic aspects for CO_2 reforming of methane over Ni based catalysts. *Chem. Eng. J.* **2015**, *278*, 62–78. [CrossRef]
154. Slagtern, A.; Schuurman, Y.; Leclercq, C.; Verykios, X.; Mirodatos, C. Specific features concerning the mechanism of methane reforming by carbon dioxide over Ni/La_2O_3 catalyst. *J. Catal.* **1997**, *172*, 118–126. [CrossRef]
155. Tsipouriari, V.A.; Verykios, X.E. Kinetic study of the catalytic reforming of methane with carbon dioxide to synthesis gas over Ni/La_2O_3 catalyst. *Catal. Today* **2001**, *64*, 83–90. [CrossRef]

156. Tsipouriari, V.A.; Verykios, X.E. Carbon and oxygen reaction pathways of CO_2 reforming of methane over Ni/La_2O_3 and Ni/Al_2O_3 catalysts studied by isotopic tracing techniques. *J. Catal.* **1999**, *187*, 85–94. [CrossRef]
157. Moradi, G.R.; Rahmanzadeh, M.; Sharifnia, S. Kinetic investigation of CO_2 reforming of CH_4 over La-Ni based perovskite. *Chem. Eng. J.* **2010**, *162*, 787–791. [CrossRef]
158. Singh, S.; Prestat, E.; Huang, L.F.; Rondinelli, J.M.; Haigh, S.J.; Rosen, B.A. Role of 2D and 3D defects on the reduction of $LaNiO_3$ nanoparticles for catalysis. *Sci. Rep.* **2017**, *7*, 10080. [CrossRef]
159. Hu, Y.; Wang, X.; Tan, M.; Zou, X.; Ding, W.; Lu, X. Perovskite $LaNiO_3$ Nanocrystals inside SBA-15 Silica: High Stability and Anti-Coking Performance in the Pre-Reforming of Liquefied Petroleum Gas at a Low Steam-to-Carbon Molar Ratio. *ChemCatChem* **2016**, *8*, 1055–1058. [CrossRef]
160. Mabaleha, S.S.; Farshad, G.; Pranjal, K. "Recent advances in Ni-based stable catalysts for methane dry reforming: Stable catalysts' preparation review. *J. Mol. Catal.* **2023**, *547*, 113398. [CrossRef]
161. de Lira Lima, D.C.; Lemos, I.P.; Gomes, R.S.; Rodrigues, L.M.T.S.; Fréty, R.T.; Resini, C.; Junior, R.B.S.; Brandão, S.T. Study of $LaNi_{1-x}Co_xO_3$ Perovskites-Type Oxides Either Pure or Mixed with SiO_2 as Catalytic Precursors Applied in CH_4 Dry-Reforming. *Catal. Lett.* **2023**, *153*, 2137–2148. [CrossRef]
162. Nezhad, P.D.K.; Bekheet, M.F.; Bonmassar, N.; Schlicker, L.; Gili, A.; Kamutzki, F.; Gurlo, A.; Doran, A.; Gao, Y.; Heggen, M.; et al. Mechanistic in situ insights into the formation, structural and catalytic aspects of the La_2NiO_4 intermediate phase in the dry reforming of methane over Ni-based perovskite catalysts. *Appl. Catal. A Gen.* **2021**, *612*, 117984. [CrossRef]
163. Bakiz, B.; Guinneton, F.; Arab, M.; Benlachemi, A.; Villain, S.; Satre, P.; Gavarri, J.-R. Carbonatation and Decarbonatation Kinetics In The La_2O_3-$La_2O_2CO_3$ System Under CO_2 Gas Flows. *Adv. Mater. Sci. Eng.* **2010**, *2010*, 360597. [CrossRef]
164. Wang, Y.; Qian, S.; Chen, Y.; Yan, B.; Cheng, Y. Effect of the Calcination Temperature of $LaNiO_3$ on the Structural Properties and Reaction Performance of Catalysts in the Steam Reforming of Methane. *Catalysts* **2023**, *13*, 356. [CrossRef]

Disclaimer/Publisher's Note: The statements, opinions and data contained in all publications are solely those of the individual author(s) and contributor(s) and not of MDPI and/or the editor(s). MDPI and/or the editor(s) disclaim responsibility for any injury to people or property resulting from any ideas, methods, instructions or products referred to in the content.